COMPUTATIONAL METHODS AND TISSUE TARGETED GENE THERAPY APPLICATIONS IN CARDIOVASCULAR DISEASE

A

Dissertation

Presented to

the faculty of the School of Engineering and Applied Science

University of Virginia

---

in partial fulfillment

of the requirements for the degree

Doctor of Philosophy

by

Christopher Waters

December 2023

This

Dissertation

is submitted in partial fulfillment of the requirements
for the degree of

Doctor of Philosophy

Author: 

This Dissertation has been read and approved by the examing committee:

Advisor: Brent A. French, PhD

Advisor:

Committee Member: Frederick H. Epstein, PhD

Committee Member: John A. Hossack, PhD

Committee Member: Thomas H. Barker, PhD

Committee Member: Kenneth C. Bilchick, MD

Committee Member:

Committee Member:

Accepted for the School of Engineering and Applied Science:

Jennifer L. West, School of Engineering and Applied Science

December 2023

ACKNOWLEDGEMENTS

To everyone who has assisted me along this journey, I express my sincerest thanks. The work presented here was not the result of only my own time, focus, and commitment, but that of many others.

A heartfelt thanks to Dr. French, who has been an understanding, wise, and brilliant advisor to learn from. His insights have been invaluable in solving any number of problems that have faced me along this path, and his support has enabled me to pursue endeavors in which I truly took great personal interest. To my committee, who have provided feedback and guidance when it was needed, and have helped steer the work presented here. To collaborators, providing insight and unique views to work together towards common solutions. The collaborators who have provided significant input are indicated here, with the chapter in which their work was invaluable:

Thien-Khoi Phung: Chapter II. TK's assistance and knowledge in the development of patient-specific LV geometries was a springboard from which all of the co-registration work could be seen through to finish.

Fady Attia: Chapters III and IV. Fady has been an invaluable undergraduate researcher and peer. From long hours working through tedious protocols and late hours huddled up against a microscope, the work you have put in has been vital in the development of this dissertation.

Lanlin Chen: Chapter IV. Without Lanlin's steady hand, none of the work in Chapter IV would be possible. Her expertise in surgical procedures is an invaluable asset not only for my work, but for the French lab as a whole.

To my labmates, Alyssa Becker and Samuel Sklar. Alyssa was a mentor in the most important moments of my graduate path, and taught me so much about handling myself as both a graduate student and member of the lab.

Sam has become more than just a labmate, and through long COVID projects and late writing nights, has become a dear friend. While his opinions and advice have been of immense value for research, his friendship has made the past few years an absolute joy.

To my friends who knew me before all of this even began, your support has been a life raft that was always available. To my family, you have always been a rock of support, such that I have never once been afraid to take a risk. I cannot ever explain how much I appreciate all that you have done for me.

And to Ana Estrada, you have been the light at the end of a very long tunnel. Your support, guidance, and care has been so uplifting. Thanks to you, I do believe that we can do anything together.

CONTENTS

CHAPTER I. DISSERTATION INTRODUCTION AND SPECIFIC AIMS

It is estimated that approximately 3.0% of the US population over the age of 20 has experienced myocardial infarction (MI) at least once, and the annual incidence rate of MI in the US has exceeded 600,000 new cases and 200,000 recurrent cases[1]. Economically, this translates to costs of approximately $29.8 billion in direct medical expenditures[2], while effective prevention and treatments could significantly reduce both the cost-per-incidence and total number of incidences. Downstream effects of MI caused by complications as a result of myocardial scar formation and remodeling result in an incidence rate of heart failure of 18.8% within 5 years of MI[3]. It is therefore of great benefit, both financially and as a matter of global health, to identify therapeutic approaches designed to reduce the long-term adverse effects of MI.

The etiology of heart failure Id as a resulI of MI is typically defined in terms of left ventricular (LV) remodeling and extent of infarcted myocardium. Changes in LV volumes and ejection fraction (EF) have each been established as independent clinical predictors of long-term risk of mortality and progression into heart failure[4–7]. Additional studies have shown that infarct size as measured by late gadolinium enhanced (LGE) CMR correlates well with post-MI changes in LV end-systolic volumes (ESV) and EF in both human patients and animal models[8–11]. As a result, care should be taken to consider each potential element of long-term LV remodeling when assessing the efficacy of potential treatments.

Computational 3D cardiac models derived from patient-specific left ventricular geometry have been shown to act as potent tools for improving diagnosis and treatment[12]. While the clinical relevance of these models is apparent, their use in preclinical settings is less common, even while routines have been developed to integrate data from a multitude of cardiac magnetic resonance (CMR) techniques[13]. Novel pulse sequences and higher-field strength MR scanners capable of measuring high-resolution regionally varying data across the entire heart are being developed[14],

but spatial registration of the resulting data typically relies on rough approximations and manual mapping from one source to the next, rather than using automated platforms for registration.

Unlike *in vivo* approaches, *ex vivo* histological methods still heavily rely upon techniques that are largely incompatible with whole-heart modeling. Our lab has made recent developments in tissue clearing protocols that have significantly improved our capability to assess whole hearts with immunohistochemistry (IHC) *ex vivo* using thick (0.5-1 mm) tissue sections. To take advantage of these novel techniques, I aimed to develop a 3D modeling platform to integrate CMR-derived and whole-heart histological endpoints to achieve a multi-scale assessment of post-MI outcomes that unites the MR-derived LV function with tissue structure at the microscopic level. This platform presents significant potential in assessing the impact of inducible nitric oxide synthase (iNOS) expression on post-MI recovery.

While we have previously established a link between global iNOS expression and post-MI function[15], but we can now investigate regional and cell-specific variations in iNOS expression using advanced gene therapy and improved analytical techniques. Spatial co-registration between functional and structural changes after MI and high-resolution cellular and molecular images using novel modeling techniques is what permits this level of analysis. The series of studies described here utilize cell type-specific iNOS knockout mice, which underwent left anterior descending (LAD) artery occlusion to induce MI, followed by reperfusion. An AAV vector driving cardiac-specific expression of Cre recombinase along with a loxP-flanked (floxed) iNOS mouse model enabled us to perform cell-specific knockout of iNOS expression.

In pursuit of the development and implementation of adaptable and user-friendly methods for preclinical assessment of cardiac-directed therapies for MI and subsequent progression of heart failure, this dissertation addresses the following two specific aims:

Specific Aim 1. Develop co-registration techniques to align 3D CMR and confocal-derived tissue models in a semi-automated platform. Combined 3D CMR models were already under development, but inclusion of confocal-derived tissue information had yet to be accomplished. Tissue clearing protocols based on advanced CUBIC and SUT protocols were optimized for use with cardiac samples, permitting confocal microscopy to be used for data collection in thick tissue sections. IHC protocols were optimized for thick tissue sections to produce evenly distributed staining with significantly improved dye penetration depths. The 3D models from both CMR and confocal microscopy were integrated into a combined 3D finite element model with the goal of assessing the spatial correlation of functional impacts of MI with biomarkers of oxidative and cellular stress. Approaches and results for this aim are discussed in Chapters 2 and 3.

Specific Aim 2. Assess the impact of cell-type specific regulation of iNOS on post-MI myocardial recovery. The impact of cell-specific iNOS knockout was assessed using the newly developed platform in Aim 1. A mouse model featuring a floxed iNOS gene was utilized in combination with both a transgenic Cre mouse model and an AAV vector driving Cre expression to assess the impact of cell-specific iNOS knockout on myocardial recovery and remodeling following ischemia-reperfusion (I/R) injury. Transgenic mice expressing Cre inserted into the macrophage-specific lysozyme 2 gene were used to investigate macrophage-specific iNOS knockout. Cardiomyocyte-specific iNOS knockout was performed using AAV9 driving Cre expression with the cTnT promoter. Approaches and results for this aim are discussed in Chapter 4.

CHAPTER II. A COMBINED CARDIAC TOOLBOX FOR AUTOMATED CO-REGISTRATION AND ANALYSIS

Introduction

CMR-based methods for delineation of the infarct and remote region typically rely upon delayed contrast-enhanced (DCE) CMR, performed following injection of a T1-shortening contrast agent, such as gadopentate (Gd-DTPA)[16]. Identification of the border zone, however, has relied upon a variety of imaging techniques and modalities, which vary in consistency of their application across different species and MI models.

CMR-based approaches to identify the border zone have included approaches that rely upon advanced diffusion-spectrum imaging sequences performed in excised hearts, which identified the border zone as a region of increased homogeneity of myofiber network orientation and span[17]. Other techniques have utilized the already-prevalent usage of Gd-DTPA contrast-enhancement for viability assessment in the post-infarct heart, establishing a range of elevated intensity to delineate border zone and core infarct in human patients or pairing Gd-DTPA with a necrosis-specific contrast agent to separate viable and non-viable infarcted tissue in reperfused MI in rat models[18,19]. Other studies utilizing Gd-DTPA and Late Gadolinium Enhancement (LGE) CMR to identify the infarct region in swine models of coronary artery ligation suggested that identification of the border zone for finite element cardiac models was not feasible using only LGE-CMR, due to the lack of a transitionary region between the infarct and non-infarct myocardium[20].

Other methods have avoided the usage of contrast agents altogether, instead basing the classification of regions as infarct or border zone upon functional or anatomical parameters. A common metric for the identification of the border zone in studies which avoided the use of contrast agents was wall thickness of the left ventricle. Due to the frequency of wall thinning within the infarct region in MI models initiated through occlusion of the coronary arteries, the border zone in these cases is defined as the region where wall thickness transitions from that seen in non-

infarcted hearts to the thinned infarct regions[21–25]. A notable weakness of these identification methods is their limited utility following ischemia-reperfusion injury, as thinning is significantly reduced in the infarct region during the inflammatory phase of post-MI recovery in reperfused MI compared to permanent ligation[26].

Tagged MRI images for strain assessment have been used in sheep models of LAD ligation to identify regions of linearly-varying strain as border zones marking the transition between the normally-functioning remote and impaired infarct regions for use in finite element models of the post-MI heart[27]. Later studies by the same researchers used a smaller border zone than the estimated 3cm width proposed by their earlier study, suggesting a high variability in possible border zone width[28].

In mouse models of ischemia-reperfusion injury, particularly with occlusion durations ranging from 30 to 60 minutes, the resulting impact on wall thickness in the infarct and border zone can be variable, confounding its usage as a method to identify border zone width. Comparisons of wall thickness at days 14, 21, and 28 in I-R injury models of post-MI remodeling following transient occlusion versus permanent ligation of the LAD have previously found no significant difference in wall thickness between remote and infarct wall regions in I-R models, while permanent ligation models exhibit far greater thinning of the infarct wall[29–31]. Especially when considering the potential benefits of post-MI therapies on LV remodeling, wall thickness as a metric to identify the infarct border zone could result in improper assignment. User-defined border zone widths allow users to tune border zone sizes alongside mesh densities to balance the platform to their needs, and that was the method we pursued here, performing an initial comparison of results across various border zone widths before identifying a preferred width based on results and visual observation.

Methods

For a visual overview of the process used in the Combined Cardiac Toolbox (from here referred to as CoCaToo), Figure 1 presents the complete alignment process from initial data collection to final combined model. Initial patient-specific LV geometries are based upon high-resolution short- and long-axis black-blood cine images, spanning the entire cardiac cycle, following previously-described procedures[32]. The animal protocol used in this study was approved by the University of Virginia Animal Care and Use Committee (Protocol 2802) and conformed to the Guide for the Care and Use of Laboratory Animals (ILAR; Revised 2011).

FORMATION OF SUBJECT-SPECIFIC LEFT-VENTRICULAR GEOMETRIES

Endocardial and epicardial contours from each of black-blood image are manually segmented using Segment by Medviso[33]. Pinpoints are placed to identify the base and apex of the left ventricle within the long-axis view and the insertion points of the right ventricle into the left ventricular myocardium within the short-axis view. Figure 2 presents the typical interface provided by commonly-used segmentation software to perform the manual segmentation

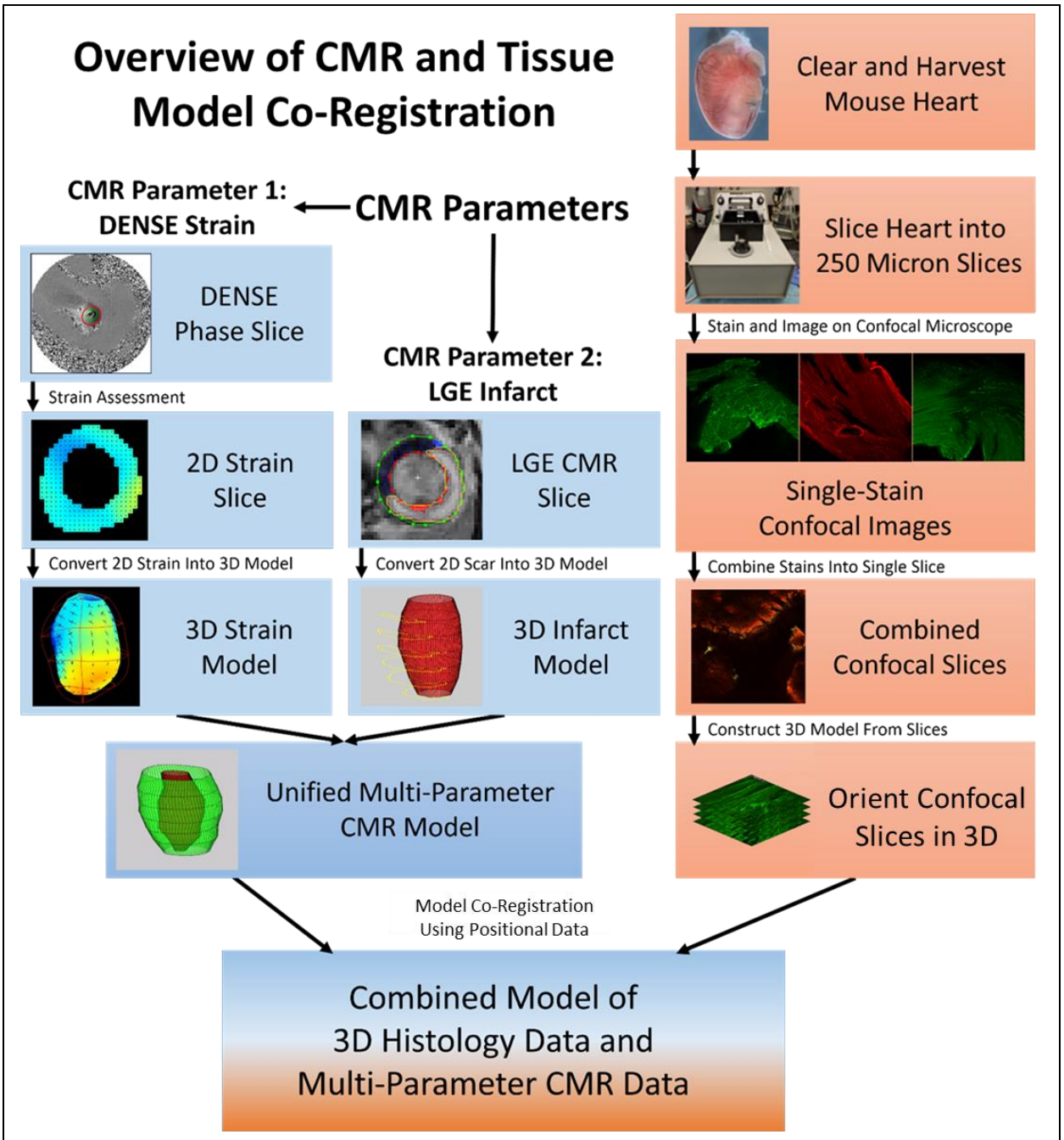

Figure 1. Overview of Combined Cardial Toolbox alignment. Base geometry is defined from cine black-blood short-axis and long-axis images. Other CMR-based data is aligned automatically using contour position, image metadata, and pinpoints for rotational correction. Confocal-derived data is aligned using user input to identify slice position, and manually-drawn contours and pinpoints are used to identify relevant data and perform alignment.

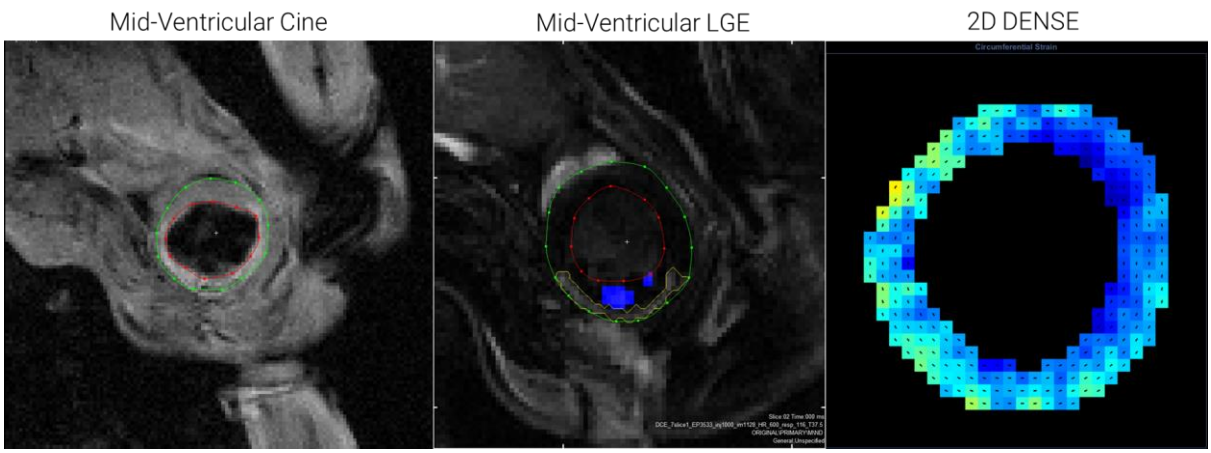

Figure 2. Input Data Formats for CoCaToo. Cine slices as shown in the leftmost panel are segmented using Segment by Medviso, along with LGE-derived scar contours as shown in the center. DENSE-based data is analyzed using the DENSEanalysis package and exported using open-source MATLAB data files.

used for model-based alignment. Two independent bicubic hermite surfaces are then fit to the endocardial and epicardial geometries in prolate spheroidal coordinates, respectively acting as the endocardial and epicardial surfaces for the finite-element model[32,34,35]. This coordinate system is defined by λ, an angle spanning from apex to base of the heart, θ, an angle defining rotation around a central vertical axis, and μ, which acts in a manner similar to a radius, defining the distance of a point from the central axis. The relationship between the prolate spheroid and cartesian coordinate system is shown in Equation Set 1. An additional component, the focus, can be considered as a scaling factor and additionally defines the height of the focal axis which acts as the center of the spheroid. The benefit of this coordinate system for the assessment of LV geometries is the relatively linearity of the ventricular contours when assessed in prolate spheroidal coordinates, easing computational complexity of interpolation techniques and co-registration.

The nodes of the finite element model are evenly distributed within prolate spheroid coordinates based on end user-defined element densities in the circumferential, longitudinal, and radial

directions. The resulting finite element model is the base model onto which all patient-specific data is projected and is the basis for 3-dimensional co-registration of functional and anatomical results.

AUTOMATED CO-REGISTRATION OF INFARCT LOCATION

Infarct locations were assessed using LGE CMR, segmented manually using Segment[36] based on elevated image brightness within the myocardium in T1-weighted images. Endocardial and epicardial contours, as well as RV insertion points, image metadata, and a binary mask indicating the infarct region, are used to align the LGE-based infarct to the black-blood-based geometry at end-diastole. The transmurality and depth of the infarct region are assessed at regularly spaced intervals along the rotation around the central point within each slice of the image stack and are then used to fit two radial basis functions, one for transmurality and one for depth, in the common cardiac coordinate system, as previously described[13]. These radial basis functions are then used to interpolate between slices in prolate spheroidal coordinates to identify individual elements of the model as either infarct or non-infarct elements.

IMPLEMENTATION OF BORDER ZONE IN COCATOO

Classification of border zone elements was performed using an iterative assignment method based on resulting infarct location and a custom-selectable "border width" metric. Initial border zone elements are established as all non-infarct elements which are immediately adjacent to infarct

$$x = a \sinh \mu \sin \lambda \cos \theta$$

$$y = a \sinh \mu \sin \lambda \sin \theta$$

$$z = a \cosh \mu \cos \lambda$$

Equation Set 1. Relationship of prolate spheroidal coordinates to cartesian coordinates. List of equations to convert from prolate spheroid to cartesian coordinate system. a is the focus of the prolate spheroid, defined as a distance from the origin. For co-registration, the focus is calculated based on the distance from apex to base of the imported slices.

elements. Following initial establishment, border zone elements are expanded outwards until the number of elements between infarct and non-infarct elements by fewest-neighbor distance is equal to the "border width" metric. The use of a custom, adjustable metric was due to the previously-mentioned variability seen in border zone width as reported in studies of post-MI LV remodeling.

CO-REGISTRATION OF DENSE IN COCATOO

While both the black-blood and LGE images are assessed using the same segmentation platform, and therefore have data representations and shared coordinate systems, DENSE-based strain metrics are initially assessed using the DENSEAnalysis MATLAB packaged maintained by Jonathan Suever[37,38]. The CoCaToo interface permits selection of any number of DENSE export files in MATLAB format, which each represent a unique image position. For co-registration of

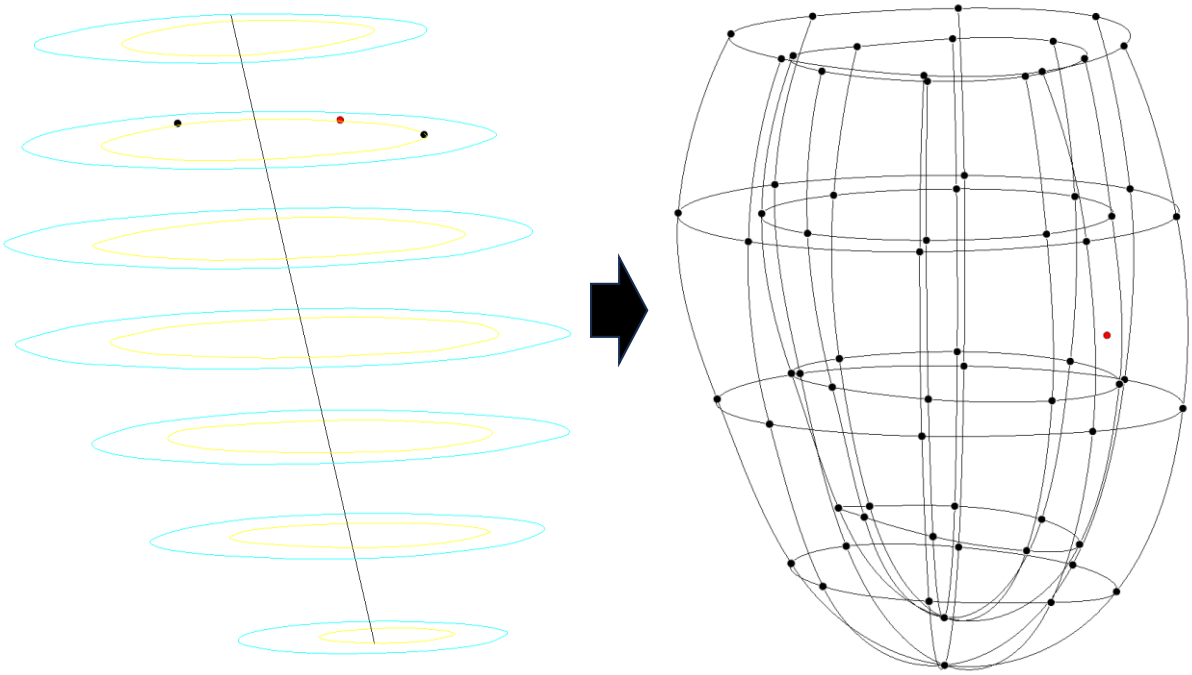

Figure 3. Co-registration surface fitting overview. Endocardial and epicardial contours are shown stacked in cartesian coordinates. Conversion to the prolate spheroid coordinate system using Equation Set 1 is performed, then independent surfaces are fit to the combined contours, as shown above.

DENSE-based strain information to the combined cardiac model, resting contours are first imported from the output of the DENSE analysis toolbox from each import file. Using these resting contours, a DENSE-based LV geometry is built and oriented using image position and orientation metadata. Contours are scaled based on the average radius of the imported resting contours for smoother interpolation and slice position-matched contours from the cine black-blood short-axis images. Data from each file containing pixel-by-pixel displacement and strain values are then imported and given positional context prior to alignment.

Each slice-based contour is then converted to the prolate spheroidal coordinate system, rotated into the common cardiac coordinate system, and used to fit a pair of cubic spline interpolations for the epicardial and endocardial surfaces, which then act as the bounds of a 3-dimensional linear gradient. The relationship between the contours and surfaces are shown in Figure 3. This 3-dimensional gradient is used to scale the positions of the pixel-based positions for strain and displacement information so that the entire point cloud is then properly aligned to the common cardiac coordinate system.

After the point cloud has been mapped into the common cardiac model, six piecewise 3-dimensional linear interpolators are fit to the data, separated by angular position around the rotational axis. The piecewise separation of the interpolators is implemented to improve fit quality in cases of extreme variance in strain values around the rotational axis, which are common in infarct models, which result in poorly-fit interpolations and high fitting errors. Each element of the finite-element model then calculates element-based strain as an average strain at each of its respective nodes. This process is then repeated for each timepoint of the DENSE cycle to get a complete timeline of DENSE-based strains and displacements in each element of the common cardiac model for which interpolation is possible. Elements for which extrapolation on any axis of

the interpolation would be necessary are assigned null values for strain and displacement and ignored for downstream processing.

CO-REGISTRATION METHODS FOR CONFOCAL MICROSCOPY IMAGES

Co-registration of confocal microscopy-based image data relies upon a custom-built segmentation platform for epicardial and endocardial labeling as well as pinpoint placement to indicate the right ventricular insertion point, accessible within the CoCaToo interface. Manual segmentation is utilized for this purpose due to the high variance across images in terms of structure and image quality resulting in a classification challenge that is poorly poised for machine learning-based image segmentation methods. CoCaToo segmentation tools were developed to have high similarity with the segmentation tools provided in Segment for ease of use. Image compression may be performed upon import of images, at a custom-selected compression factor, or to match final image resolution to DENSE or Cine images. Compression significantly reduces computational complexity of both slice fitting and data interpolation and significantly reduces the memory footprint of the model to allow co-registration to be run on commonly-available PC hardware at the expense of data resolution.

Positional information for initial contour alignment relies upon image resolution, collected from image metadata, and a user-reported slice location, provided as distance from the apex of the heart to the location of the slice in millimeters. Image z position within the common cardiac coordinate system is calculated using the ImagePosition and ImageOrientation matrices provided with from the MRI image data. The contours are rotated into the common cardiac coordinate system using the pinpoint placement, image resolution, image position, and image orientation matrices to align the contour both in position and rotation to the cine-based LV geometry. Following positional and rotational orientation, endocardial and epicardial contours are aligned to the bicubic mesh-derived

endocardial and epicardial surfaces using Akima spline interpolation. Pixels that fall between within the polygon bounded by the contours are tracked, with positions of these pixels rotated with the same transformation steps used for contour rotation.

Following import, positions are converted to prolate spheroidal coordinates to reduce computational complexity for surface fitting and improve the results of linear interpolation methods in multiple dimensions. Pixel mu values in prolate spheroidal coordinates were calculated based on a 3-dimensional linear interpolator, using λ, θ, and ratio of fitted to unfitted mu values determined from fitted endocardial and epicardial contour points. Point locations are constrained from falling within the endocardial surface or beyond the epicardial surface during interpolation.

Calculation of confocal-derived fluorescence values for the cardiac finite element model is performed using the same techniques employed in the case of mapping of DENSE-derived strain values onto the finite element model. Six piecewise linear interpolators are calculated for each model, separated using evenly spaced phi values around the central long axis of the heart. Values in each desired fluorescence channel are interpolated to all element centers that do not require extrapolation along any dimension, leaving the fluorescence values in all other elements as an uncalculated value to avoid impacting average fluorescence calculations.

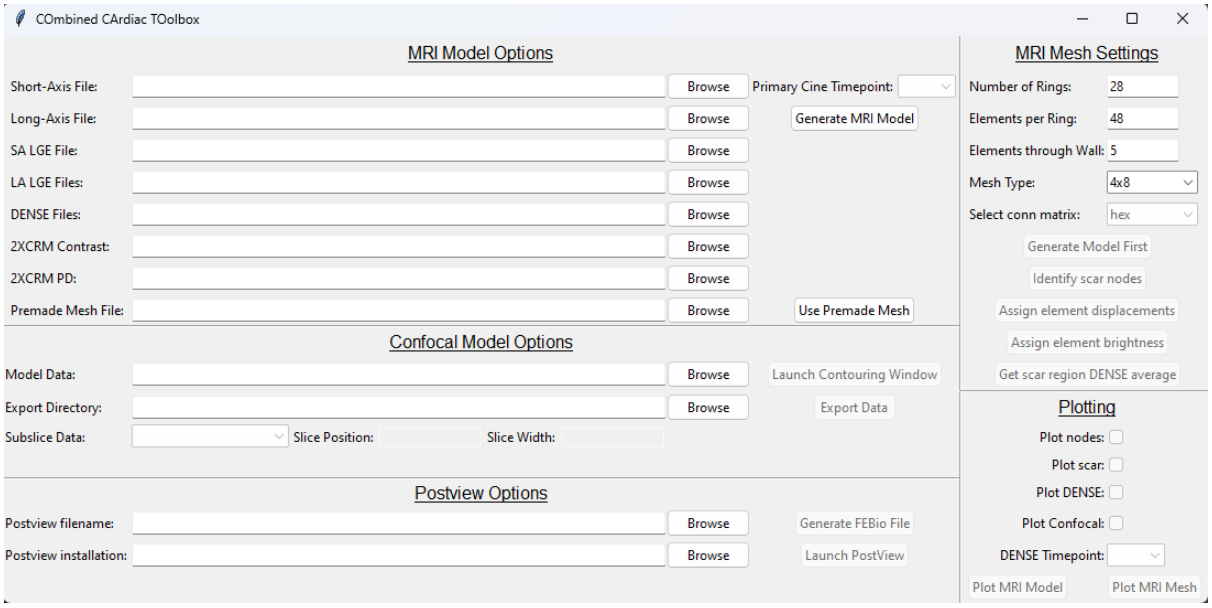

Figure 4. CoCaToo Main Interface. The GUI of the platform allows users to perform automated processing and alignment without requiring complex scripting actions. Inputs are provided to fine-tune model parameters and data inputs.

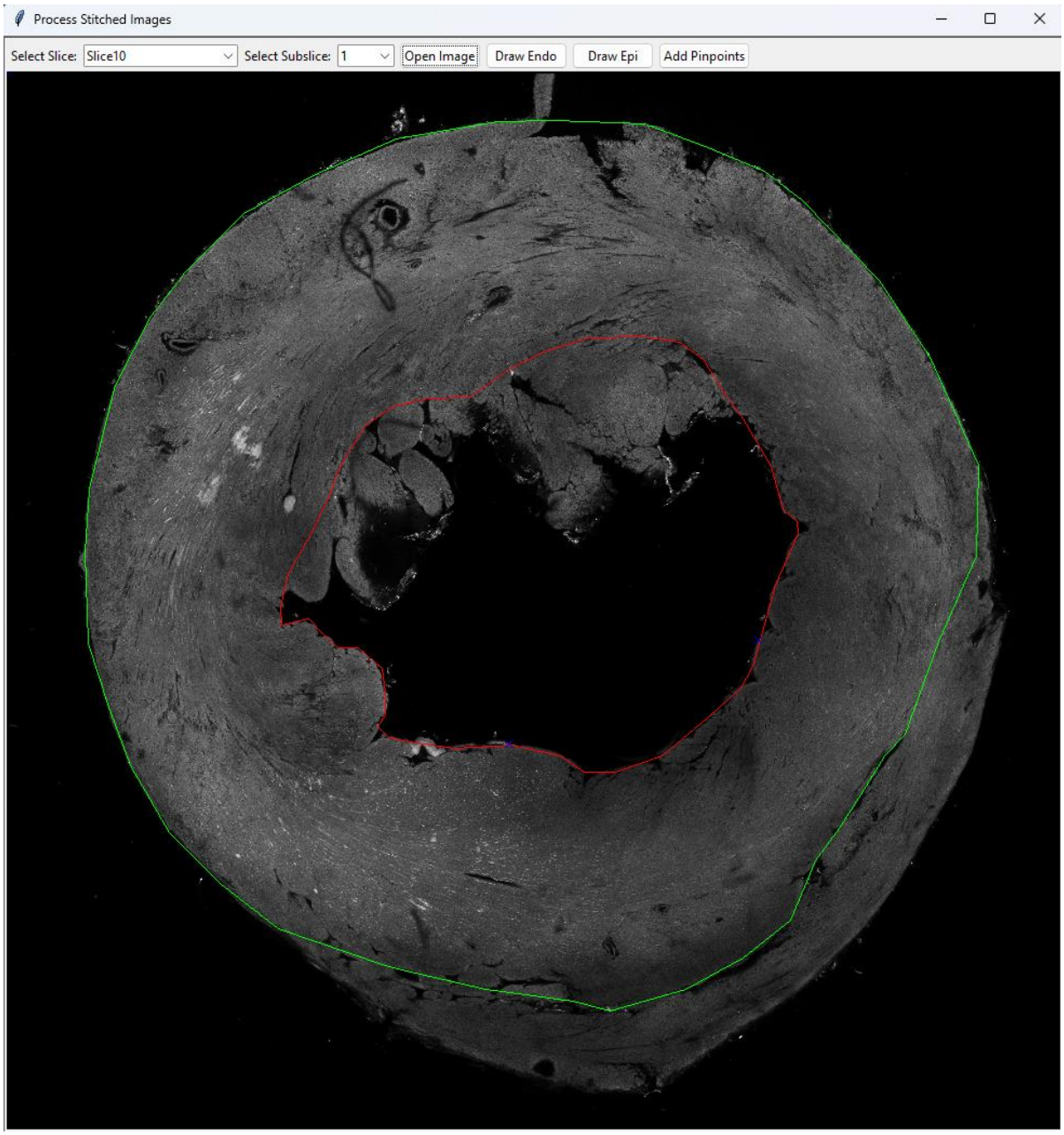

Figure 5. CoCaToo Confocal Contouring Interface. The contouring interface is designed to mirror the interface provided by Segment, due to anticipated familiarity of the interface by end-users of the platform. Contours can be edited and are automatically stored in memory. Contours and position information can be saved locally using an export option, which saves data to the folder containing the base images.

To validate co-registration of both infarct placement and DENSE, patient-specific infarct geometries were compared to randomization of element assignment to the three respective infarct geometry categories. Averaged radial and circumferential strain time courses calculated for each of the three groupings were compared between co-registration-based and randomized infarct approaches.

Validation of the interpolation of strain values was performed in each mouse by comparing against a non-piecewise linear interpolation field at the point positions used for interpolation fitting. Errors at each point were used to calculate the sum of squared error for each interpolation method in the same model, with both interpolation methods run simultaneously.

The user interface is shown in Fig GUI and contains built-in tools to assess infarct-specific strain with a single click, requiring no additional software development by the end-user.

The Common Cardiac Toolbox (CoCaToo) was developed as a robust, user-friendly graphical interface to permit interaction with the combined multimodal cardiac model described within this chapter. The interface requires no manual scripting on the part of the end-user, instead dynamically adjusting model parameters based on selected data files and textbox-based inputs. The interface, shown in Figure 4 was designed to permit users to view 3-dimensional representations of the input data to confirm alignment and view the resulting combined cardiac finite element model with built-in visualization tools. The confocal microscopy-specific segmentation interface, shown in Figure 5, automatically exports model and slice data, including position and contour information, into a custom data file to allow for rapid reimport without the need to perform segmentation steps any additional times. Users may also export resulting cardiac geometries into an FEBio-compatible geometry file, which can be used for assignment of material properties for downstream simulation.

Results

CONFIRMATION OF CO-REGISTRATION OF DENSE AND LGE VERSUS RANDOMIZATION

In order to confirm co-registration of DENSE-derived strains onto the cine-based finite element model, a comparison between co-registered and randomized element assignment was performed using 103 separate imaging sessions, each of which contains short- and long-axis black-blood cine images, short-axis LGE images, and three slices of 2D DENSE imaging taken at the three slices nearest to the mid-ventricular slice location. Models were created using an automated script, which imported manually-segmented data from each imaging sequence for co-registration. Additionally, at each time point, following co-registration and export of DENSE-based strains separated by the infarct status of each element, element statuses were randomized, and strains were recalculated based on these random assignments. In cases of randomized element assignment, no difference is observed between grouped element results, with each "region" average falling near the global mean, while alignment produces contiguous element clusters with consistent and expected results within groupings. Representative examples of mesh mapping of infarct and strain data is shown in Figure 6.

ASSESSMENT OF INTERPOLATION METHODS FOR STRAIN CO-REGISTRATION

The errors resulting from linear interpolation of strain across the myocardium in prolate spheroidal coordinates were compared between a single 3-dimensional linear interpolator and the novel 6-component piecewise linear interpolator by strain derived from interpolator calculation to known ground-truth strain at each timepoint. Root-mean-squared error was calculated for each model in each time point at which DENSE

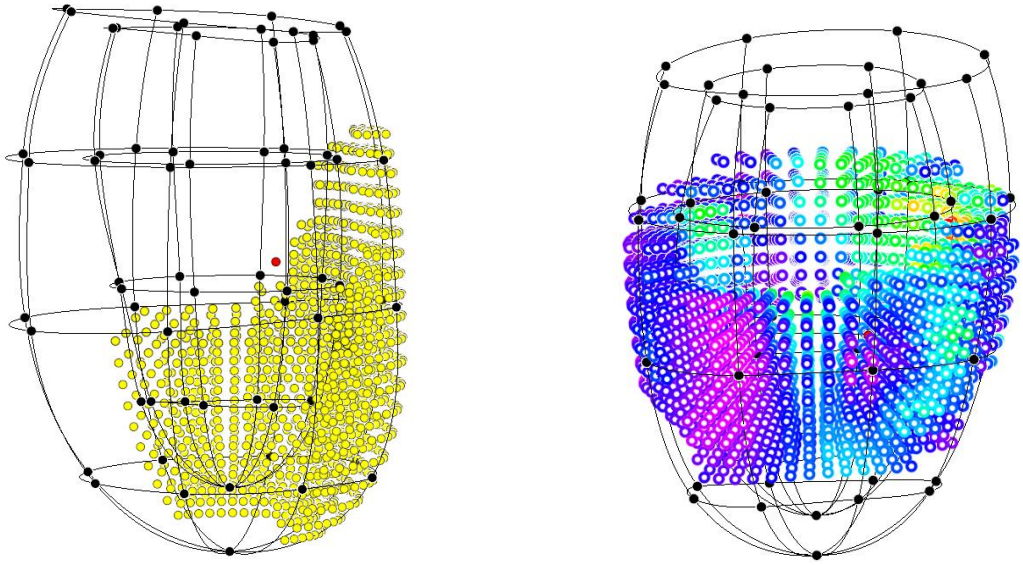

Figure 6. CoCaToo Mesh Plots. Infarct nodes (left) and elements within the DENSE interpolation field (right) can be plotted to confirm alignment and proper coregistration. DENSE plots can be provided with a timepoint within the cardiac cycle to assess spatial distribution of strain with a colormap plot.

was captured and averaged across all mice and timepoints used in the study. For the single linear interpolator, average root-mean-squared error was 0.262 ε in the case of radial strain and 0.144 ε in the case of circumferential strain. For the novel piecewise linear interpolator, average root-mean-squared error was 3.62×10^{-16} ε in the case of radial strain and 2.58×10^{-16} ε in the case of circumferential strain.

Discussion

The difference in RMSE of approximately 15 orders of magnitude between the two interpolation methods used for DENSE strain interpolation can largely be explained by the nature of the relationship between strain values, myocardial infarction, and their distribution along θ in the common cardiac coordinate system. While strains are typically well-synchronized along this axis in healthy hearts, magnitudes and onset of contraction vary significantly between healthy and infarcted myocardium[39]. The immense variation results in a trend that is not well-suited for a linear interpolation along the θ dimension. Due to available interpolation methods in Python and commonly-used scientific and mathematical analysis packages, interpolation above 2 dimensions is limited to linear methods. As these packages were used to develop the combined CMR cardiac model, the most reasonable approach was determined to be a 6-segment piecewise interpolator to balance the quality of fitting against computational complexity.

One key limitation of the model as it is currently designed is the reliance on image metadata as an alignment tool for co-registration of DENSE data. While infarct geometries are co-registered using similar landmark-based registration methods, the DENSE analysis toolbox does not output this information, thereby limiting analysis of DENSE data to images captured during a single imaging session without moving the patient between the capture of cine and DENSE images. This may

introduce a notable restriction in cases where animals are unable to endure the stress of particularly long imaging times required for DENSE.

The current method for co-registration of the infarct geometry onto the combined CMR model relies upon conversion of scar extent to only two metrics: transmurality and depth. While not yet implemented in the model, the adaptation of the 3-dimensional fitting method developed for the DENSE-based point cloud to the challenge of infarct co-registration could provide improved fitting results not reliant upon dimensional reduction.

The challenge of co-registering confocal microscopy-derived fluorescence data to the CMR-derived LV geometry is a multi-pronged challenge, centered on the notable differences in scale of the input data, lack of positional information for image position compared to CMR, and irregularity of LV geometry in histological sections. While mounting strategies can be adjusted to produce more regular histological sections, these processes only serve to mitigate the problem. While many histological samples used in the process of fine-tuning the co-registration were sufficiently regular and could be easily fit, several samples were removed from the fitting process due to either prominent tearing artifacts within the sample or partially-folded myocardium, which precludes contouring approaches to indicates the epicardial and endocardial surface.

CHAPTER III. UPDATED PROTOCOLS FOR CARDIAC-SPECIFIC TISSUE CLEARING AND HISTOLOGICAL METHODS

Introduction

While techniques for *in vivo* data collection have been rapidly developed and adopted over the past several decades within the preclinical setting, *ex vivo* analysis has failed to progress as rapidly. Generation of 3D mesoscale models of histological data has relied upon adoption of *in vivo* techniques to bridge the gap, sacrificing the high resolution of data that is typical of *ex vivo* microscopy techniques. One method used to smooth co-registration of *in vivo* and *ex vivo* images with regards to CMR is the implementation of 3D-printed scaffolds to preserve heart shape after excision for *ex vivo* MRI[40,41]. While these approaches can aid in bridging the gap between resolutions, implementations still eventually hinge upon cross-modality co-registration if *ex vivo* microscopy is necessary and can be further complicated by the need to co-register cardiac surfaces across imaging sessions.

A common technique in mesoscale microscopy approaches for thick tissue sections is blockface processing, which relies upon the imaging of serial sections in embedded whole tissue samples, performed by removing tissue layers between microscopy of exposed tissue surfaces. Blockface approaches rely upon specialized hardware to maintain sample alignment and positional information between image acquisition, often using automated stage systems which permit imaging and layer removal without removing the sample from the microscopy environment. Mechanical approaches for blockface layer removal have been pursued in the brain using cryosectioning techniques on postmortem human samples paired with digital microscopy[42] and submerged agarose-embedded tissue samples processed with a vibratome paired with two-photon tomography for the development of a connectome atlas[43]. Serial blockface histology has been used in contexts beyond neurological imaging as well. A similar method has been performed in cardiac

tissue samples by pairing a confocal microscope with both an automated ultramill[44,45] and an ultramicrotome[46], capable of removing thin layers of myocardium between image acquisition.

While mechanical blockface approaches are still improving, additional advancements in laser-based ablation methods have been extended for use in serial sectioning as well. Novel approaches utilizing ultrashort high-power laser bursts can produce fine-tuned tissue layer removal without damage to the underlying or surrounding tissue[47]. These techniques have been leveraged in the development of an angiotome of *C. elegans*, using a commercially available system paired with a two-photon imaging system to produce serial sections with a slice width ranging from 50-150 μm[48]. A related approach utilizing focused ion beam milling for tissue layer removal has been shown to be capable of removing as little as 70nm of tissue when paired with scanning electron microscopy[49], which establishes the potential for blockface approaches to be used even in nanoscale-level imaging. While this entirely-optical system removes the need for mechanical processing, which can introduce tissue deformation, it still necessitates the use of a specialized platform to perform serial ablation procedures during imaging to maintain positional alignment of serial image slices. Additionally, the cost of such setups typically far exceeds that of mechanical slicing methods, and laser ablation methods result in irreversible loss of tissue samples, while mechanically-sliced sections could potentially be retained for additional follow-up processing and imaging.

Serial blockface histology has notable benefits in the ease of registration and alignment of serial histological samples and minor to non-existent deformation of tissue samples as a result of slice processing. Drawbacks of these methods include the relative incompatibility with immunohistological techniques, as access to the inner regions of the thick tissue sections with antibody-bound fluorophores is reliant upon lengthy perfusion-based approaches, which

significantly impact costs due to the high volumes of staining media required and complex perfusion apparatuses depending on the organs of interest. Typical IHC methods utilizing both primary and secondary antibodies further extend the time required for perfusion. Additionally, even several mechanical slicing methods result in complete loss of tissue samples over the course of image acquisition, precluding samples from being used for additional histological assessment or being preserved for confirmation of histological results. As a way to mitigate these potential downsides and for cases where combined sectioning-imaging platforms are unavailable or impractical to use, optical sectioning techniques can be implemented as an alternative.

The development of optically-transparent tissue sections for histological analysis has been pursued within the scientific community for over a century, beginning with the first translucent human tissue samples produced by Werner Spalteholz[50]. One key advancement that reignited interest in tissue clearing protocols was the development of light-sheet fluorescence microscopy (LSFM), permitting more rapid imaging of whole-mount organ samples and improved image quality at greater depths into tissue samples[51]. Computational processing capabilities had additionally progressed to the stage at which organ-scale microscopy-derived images were practical for analysis. As a result, advancements in tissue clearing protocols occurred rapidly, particularly with a focus on neuronal tissue and whole-brain imaging. Early clearing reagents, such as Benzyl Alcohol / Benzyl Benzoate (BABB) were used to clear whole mouse brain samples to build a more comprehensive connectome atlas.

Protocols were soon developed with the express purpose of whole-mount brain clearing, each attempting to solve various challenges of light scattering, tissue deformation, rate of clearing, and fluorescence retention. Sca*l*e was a protocol initially designed to limit light scattering in whole-brain samples and was tested using LSCM, but was extremely slow and resulted in loss of

endogenous fluorescent proteins[52]. It has since been updated to a newer protocol, Sca*l*eS, designed to maintain greater tissue integrity throughout the clearing procedure, improve clearing speed, and retain lipid-bound dyes after clearing[53]. As other protocols, such as 3DISCO, SeeDB, CLARITY, and Clear^{T} were developed, brain-specific clearing and imaging using LSFM was retained as the primary focus[54–57]. Whole-brain clearing had fewer complications than were present in other tissues of interest, such as the light-absorbing properties of hemoglobin and myoglobin in the visible spectrum[58].

Protocols which were developed with a specific focus on whole-body or non-brain organ clearing included the Clear, Unobstructed Brain/Body Imaging Cocktails (CUBIC)[59–61] and Scheme Update on Tissue Transparency (SUT)[62] procedures, which have been specifically adapted for use in cardiac tissues. A perfusion-modified variant of CUBIC, referred to as CB-Perfusion, saw marked improvements in heart transparency and compatibility with 3D-Immunohistochemistry methods[63]. As tissue permeability to antibody staining was still a challenge, further advancements on the CUBIC protocol were made to improve its performance in cardiac-specific applications involving IHC, which suggest that imaging depths of up to 250 μm are possible in cleared cardiac sections[64].

Optical sectioning techniques were preferable over blockface methods for the specific use-case in post-MI cardiac tissue to preserve sample geometry during processing and reduce the need for specialized equipment and intermediate imaging techniques for geometric alignment. Implementation of these methods can inform novel approaches to assess cardiac structure and function both *in vivo* and *ex vivo* using multiple image modalities while still producing a single combined 3D model for co-registration and analysis. It was therefore important to identify optimized tissue clearing protocols for cardiac tissue transparency while retaining maximal

fluorophore brightness through completion of imaging procedures. In addition to two existing protocols which showed the highest promise based on published results, CUBIC and SUT, a new protocol, Cardiac-Specific Advanced CUBIC, was developed to attempt to leverage the strengths of both clearing protocols.

Methods

The animal protocol used in this study was approved by the University of Virginia Animal Care and Use Committee (Protocol 2802) and conformed to the Guide for the Care and Use of Laboratory Animals (ILAR; Revised 2011).

CANDIDATE PROTOCOLS

1) Clear, Unobstructed Brain Imaging Cocktails (CUBIC)

Reagents:

CUBIC-I: 25% w/w urea, 25% w/w Quadrol (Millipore-Sigma; Burlington, MA), and 15% w/w Triton X-100 in dH2O.

CUBIC-II: 25% w/w urea, 50% w/w Sucrose, and 10% w/w nitrilotriethanol in PBS.

Protocol:

Initial clearing trials were performed using the Advanced CUBIC Protocol[59], which was initially designed for neural tissue clearing prior to adaptation to other tissue types:

1) Mice are heavily anesthetized using a mixture of ketamine and xylazine (60 mg/kg b.w. and 5 mg/kg b.w., respectively) and death is confirmed via bilateral thoracotomy.

2) Hearts are perfused with 4% paraformaldehyde (PFA) in PBS for 10 minutes and extracted by clipping the heart at the upper portion of the atria.

3) Harvested hearts are incubate overnight in 4% PFA in PBS for post-fixation.

4) Hearts are briefly washed in PBS and transferred to incubation in a bleaching solution of 7.5% hydrogen peroxide in ethanol until all pigmentation is visibly eliminated, typically 10 weeks.

5) CUBIC-I until optical clarity is reached, typically 7-14 days, for delipidation. CUBIC-I solution is replaced every 2-3 days as needed.

6) If needed, hearts are incubated in staining solution for 1 day.

7) Hearts are transferred into CUBIC-II to perform refractive index matching for 1-2 days before slicing and imaging.

2) Scheme Update on Tissue Transparency (SUT)

Reagents:

SUT Solution: 25% w/w urea, 15% v/v Triton X-100, and 8% w/w sodium dodecyl sulfate in PBS.

The Scheme Update on Tissue Transparency[62] protocol was developed specific to cardiac tissue clearing with an aim of high protein retention. Following anesthesia and confirmation of death as described previously, the protocol continued as indicated, featuring slight changes compared to initially published procedures due to equipment unavailability:

1) Hearts were perfused with 40 ml of 10 U/ml heparin in PBS over a period of 20 minutes.

2) Hearts were slowly perfused with 30 ml 4% PFA in PBS to initiate fixation.

3) Heart specimens were fixed overnight using 4% PFA in PBS.

4) Hearts were washed for 2 hours in 1X PBS.

5) Incubate the hearts overnight in 4% acrylamide solution in PBS.

6) Wash hearts for 2 hours in 1X PBS.

7) Incubate hearts in 0.25% VA044 in PBS in a degassing chamber for 1 hour at room temperature.

8) Incubate hearts in 0.25% VA044 in PBS in a degassing chamber for 3 hours at 37°C for tissue-hydrogel matrix formation.

9) Incubate hearts in SUT solution, replenished daily, at 37°C until optical clarity is observed.

10) Staining procedures can be undertaken after optical clarity is observed, following an extended wash cycle and including a 2-4 day incubation period for both primary and secondary antibody staining steps.

11) Imaging should be performed rapidly after completion of staining and return of tissue to SUT, due to a negative impact of extended SUT incubation on fluorescence.

3) Cardiac-Specific Advanced CUBIC (CSAC)

The Cardiac-Specific Advanced CUBIC protocol was developed as a combination of the reagents used for advanced CUBIC clearing and the methodology for rapid initiation of fixing and clearing found in SUT. An additional perfusion step was introduced to induce tissue bleaching, inspired from a modification of the CUBIC protocol intended for whole-insect body clearing[65]. As indicated previously, mice were anesthetized and bilateral thoracotomy was performed prior to affixing an intracardial catheter for the initial perfusion steps of the protocol:

1) Hearts are perfused with 30 ml of 15 U/ml heparin and 4% PFA in PBS over a period of 20 minutes.

2) Hearts are then perfused with 30 ml of a bleaching mixture of 7.5% hydrogen peroxide in ethanol, initially intended for whole-body clearing of beetles but practical for bleaching of hemoglobin and myoglobin in mammalian tissues[65] over a period of 20 minutes.

3) Hearts are then perfused with 30 ml of 25% CUBIC-I in dH2O to rapidly initiate the clearing protocol prior to harvest and incubation in CUBIC-I.

4) CUBIC-I incubation is carried out on a nutator shaker until tissues are sufficiently clear based on optical inspection (typically ~2-3 days)

5) Staining procedures can be performed after optical clarity and delipidation have been performed, prior to incubation in CUBIC-II.

6) Hearts are transferred into CUBIC-II for refractive index adjustment and reduction of swelling (typically ~2 days). The incubation times established in this protocol represent an approximately 5-fold faster clearing time between tissue harvest and image readiness.

Following the completion of each protocol up to preparation for slicing and imaging, hearts are sliced at desired widths and mounted onto slides, covered with #1 cover glass (VWR International; Radnor, PA) and sealed using clear nail polish.

FLUOSPHERE ANALYSIS OF TISSUE CLARITY

CUBIC and CSAC clearing protocols were initially assessed using 15-μm diameter yellow-green fluorescent FluoSpheres (ThermoFisher Scientific; Waltham, MA). A 0.25ml bolus containing 2.5E5 microspheres was delivered to C57BL/6J mice via intracardiac injection following anesthetization using a mouse anesthetic mix and allowed to circulate for 3 minutes. Hearts were harvested and processed according to either the CUBIC or CSAC protocol. Samples were then embedded in a solution of 2% agarose, cooled to form a gel support structure, and sliced using a

Compresstome® (Precisionary Instruments; Natick, MA) set to 500 μm slice thickness. Samples were then mounted onto custom-made microscopy slides for thick tissue sections and imaged using a Leica Stellaris 5 upright confocal microscope using a 488-nm laser excitation with an emission filter set to 495-525 nm, using a constant laser power and detector gain across samples. For processed images, an HC PL APO 20x dry objective with a numerical aperture of 0.75 and a working distance of 0.62mm (Leica MicroSystems; Wetzlar, Germany) was used as the primary objective.

EFFECTS OF TISSUE CLEARING ON NUCLEIC ACID STAINING

Due to reported concerns of fluorescence degradation as a side-effect of incubation in the SUT solution, these hearts were not used in the FluoSpheres comparison. Instead, a comparison between SUT, CUBIC, and CSAC-cleared hearts was performed using Hoechst 33342 nuclear stain (ThermoFisher Scientific; Waltham, MA) to assess both penetration of dye and fluorescence retention. Heart samples were processed according to the previously-described protocols, with no injections or alterations prior to staining. For both CUBIC and CSAC-cleared tissues, samples were incubated in 2 μg/ml Hoechst 33342 dye in the refractive index-matching solution for the respective protocol, while SUT-cleared tissues were incubated in 2 μg/ml Hoechst 33342 in the SUT reagent.

Images were captured with a Leica Stellaris 5 upright confocal microscope with an HC PL APO 20x dry objective (NA=0.75) using a 405nm excitation diode paired with an emission filter set to 410-470nm. A comparison of brightness was performed at the surface of the tissue samples and again at a slice depth of 50 μm as an initial comparison. Brightness assessment was calculated using an automated thresholding technique previously developed for regional comparison of oxidative stress using dihydroethidium[14]. Images were normalized to local background using a 30-

pixel rolling kernel in ImageJ, which results in local maxima with uniform peak brightness. A thresholding step is performed to automate masking, identifying nuclei as local maxima against local background fluorescence, due to the rolling kernel. Cross-sample comparisons can then be performed by calculating the product of the nuclei brightness:background brightness ratio and nuclei area:total myocardial area, which results in an area-normalized brightness comparison which evenly weights the brightness of automatically-detected nuclei and the density of detected nuclei using the automated thresholding technique. These two factors are key comparison metrics for retention of fluorescence intensity at greater slice depths and successful dye penetration into the tissue sample, due to the assumption of uniform nuclei density throughout the tissue.

Results

VISUAL ASSESSMENT OF TISSUE CLARITY

Between each incubation step of the protocols, whole hearts were briefly imaged using a grid-lined background to visually assess sample clarity and adjustments to refractive index. Samples cleared using the CUBIC protocol (Figure 7) exhibited similar bleaching results at week 10 to those seen in CSAC-treated samples (Figure 8) immediately following perfusion. The extended incubations in hyperhydration solutions additionally seems to produce greater swelling of tissue in CUBIC-treated samples. SUT-treated samples (Figure 9), however, exhibit minimal change in

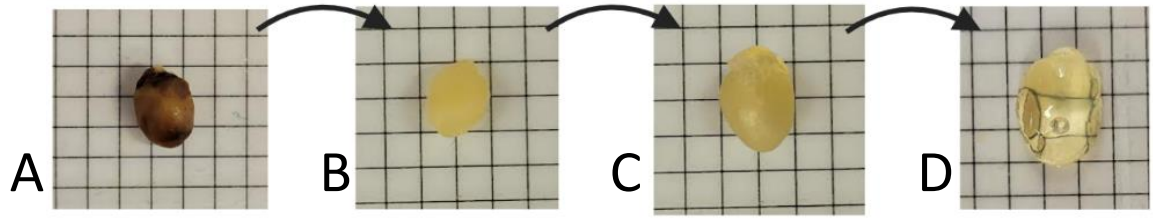

Figure 7. Visual Assessment of CUBIC Clearing. CUBIC-cleared samples were assessed at (A) extraction, (B) after bleaching, (C) after incubation in CUBIC-I, and (D) after incubation in CUBIC-II. Total duration was 18 weeks. Grid spacing is 5mm between grid marks.

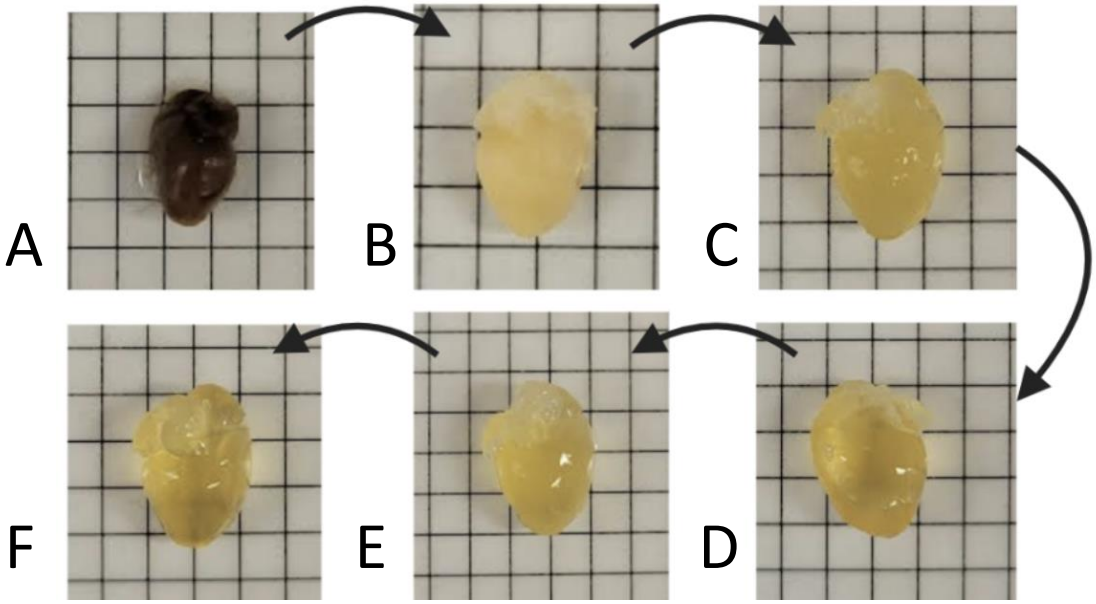

Figure 8. Visual Assessment of CSAC Clearing. CSAC cleared samples were compared to a (A) freshly-fixed heart. Observations were made at (B) extraction following perfusion, (C) after incubation in 0.5X CUBIC-I, (D) after incubation in 1X CUBIC-I, (E) after incubation in 0.5X CUBIC-II, and (F) after incubation in 1X CUBIC-II. Total duration was 6 weeks.

volume, but retain a higher concentration of apparent pigmentation, even after tissue clarity has reached desired levels.

Retention of tissue integrity was additionally considered, due to the planned use of the selected protocol alongside mechanical sectioning on a CompressTome slicer. While both CUBIC-cleared and CSAC-cleared samples retained expected slice structure following sectioning, SUT-cleared samples exhibited prominent tearing and collapse of the LV structure, which could cause complications if used for automated histological analysis in CoCaToo.

FLUOSPHERE ANALYSIS OF TISSUE CLARITY

FluoSphere brightness was compared between CUBIC-cleared and CSAC-cleared hearts using a 30 μm step size along the z-axis through the individual slices of the heart, and fluosphere brightness was assessed at each step relative to brightness at the surface of the tissue sample. FluoSphere brightness at the surface of the samples was similar between clearing protocols: CSAC-cleared

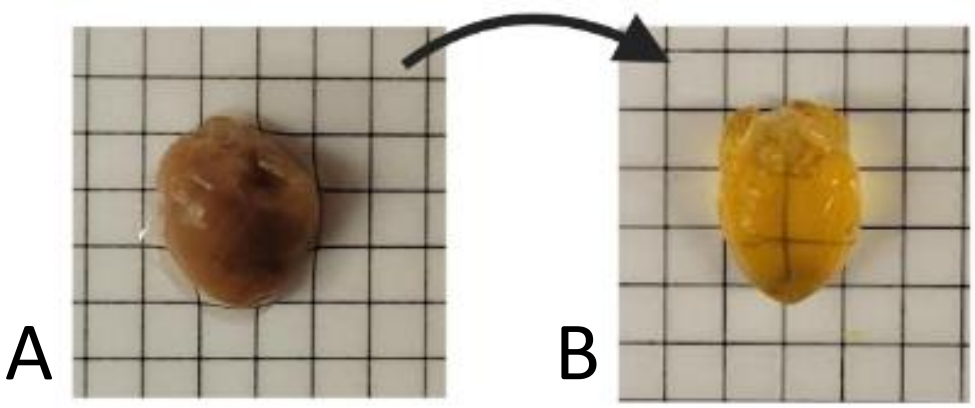

Figure 9. Visual Assessment of SUT Clearing. SUT-cleared samples were assessed at (A) extraction and (B) after completion of the SUT protocol. Intermediate steps produced no clearing during the SUT protocol. Total duration of the protocol was 9 weeks.

samples exhibited an average pixel intensity of 203.9 ± 58.2 a.u. vs CUBIC-cleared samples at 212.6 ± 54.7 a.u., measured as pixel intensity on a scale of 0-255 using ImageJ[66,67]. Brightness in each set of samples steadily decreased as images were taken at greater tissue depths, and brightness at each slice position was normalized to surface brightness and fit using a logarithmic function to describe the impact of imaging depth on fluorophore brightness, shown in Figure 10. The resulting fit in CSAC-cleared tissue samples was $Relative\ Brightness = -0.235 \ln(Depth) + 0.9217$, with R^2 = 0.818. The fit in CUBIC-cleared samples was $Relative\ Brightness = -0.368 \ln(Depth) + 0.9719$, with R^2 = 0.937. We determined an appropriate maximum tissue thickness as the depth at which brightness fell below 50% of the maximal fluorophore brightness seen at the surface of the tissue sample, which was determined to be 200 μm in CSAC-cleared and 100 μm in CUBIC-cleared samples.

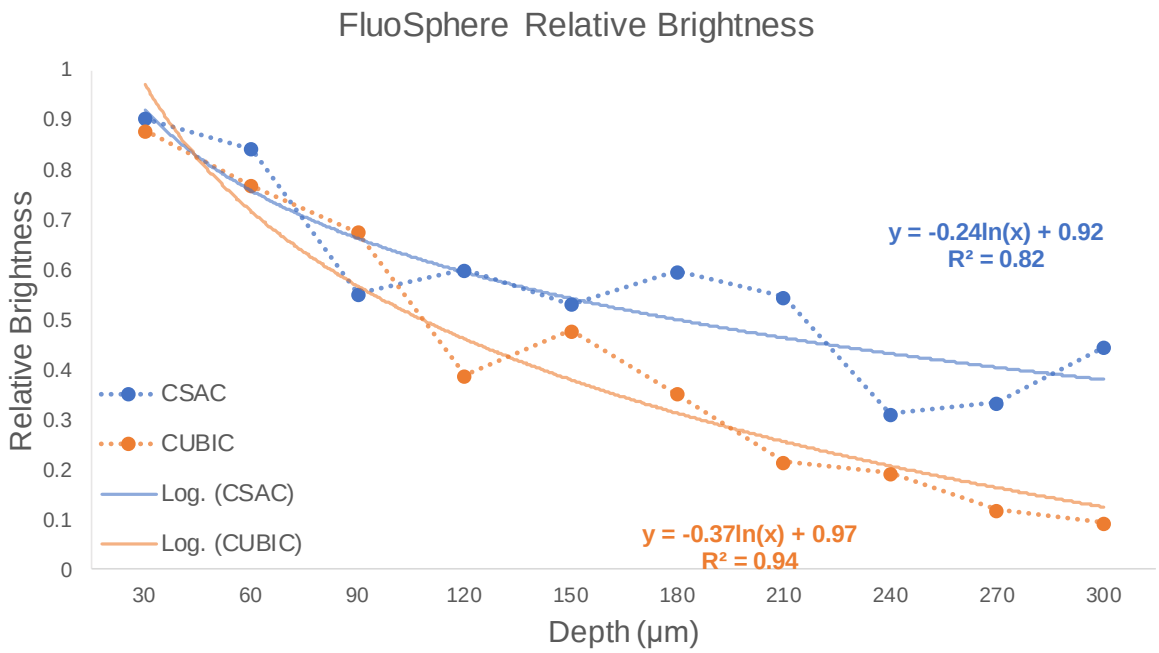

Figure 10. Assessment of FluoSphere Brightness at Sequential Image Slices. FluoSphere brightness values were normalized to that observed at the surface of the tissue in relative fluorescence units. Logarithmic trend lines were used to estimate decay for each clearing protocol to identify both relative clearing efficacy and an ideal slice thickness for imaging.

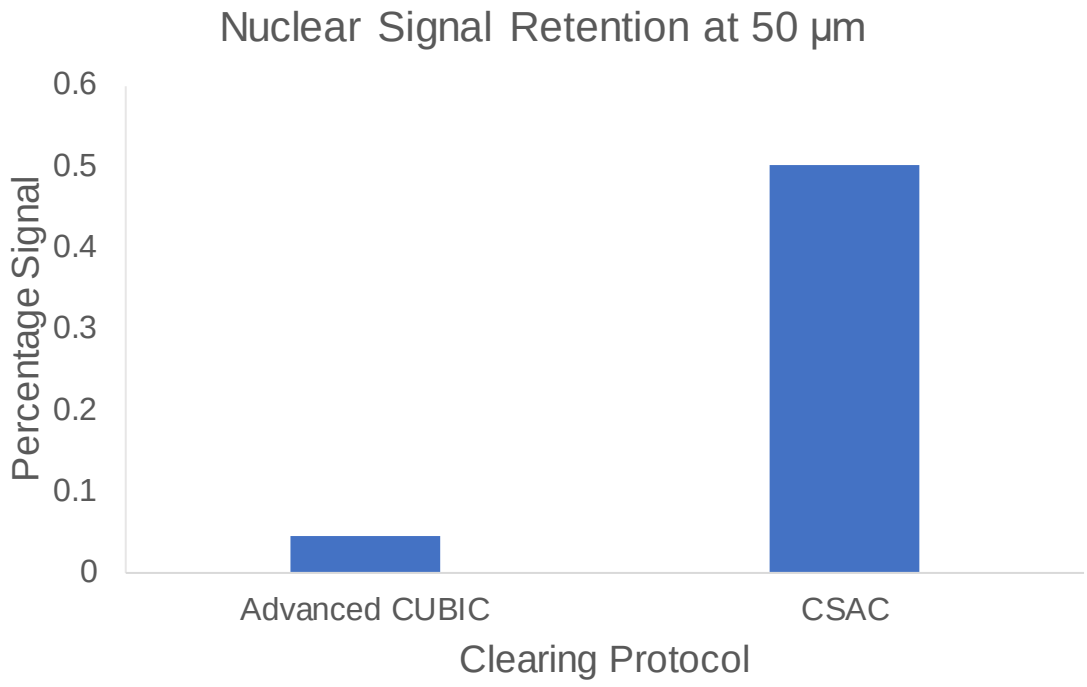

Figure 11. Assessment of Nuclei Stain Brightness at 50 µm Slice Depth. Hoecht 33342 nuclear stain was used to identify nuclei in cleared tissue samples. SUT-cleared hearts had no detectable nuclei at the tissue surface and degraded heavily upon slicing, so data was not collected other than brief visual assessment. Nuclei area-adjusted brightness was used to compare the efficacy of both stain efficacy and laser penetration to a less-fluorescent target for CUBIC and CSAC-cleared samples, with CSAC results showing improved nuclei resolution.

EFFECTS OF TISSUE CLEARING ON NUCLEIC ACID STAINING

Area-normalized nuclei brightness results for all three clearing techniques were compared at both tissue surface and 50 μm slice depths. SUT-cleared tissue samples were determined to exhibit poor stain retention even at the surface of the tissue, with a 20-fold lower peak nuclei brightness compared to both CSAC and CUBIC-cleared samples. At 50 μm penetration depth, CUBIC-cleared samples exhibited only 4.5% of the area-controlled brightness compared to tissue surface, while CSAC-cleared heart slices exhibited a 50.3% signal strength retention compared to tissue surface, shown in Figure 11.

Discussion

Published findings of cardiac-specific transparency metrics using CUBIC clearing techniques have suggested that using a 10x dry objective, brightness would not drop below 50% surface brightness until an imaging depth of approximately 400 μm, and usage of a 20x oil-immersion lens resulted in no detectable loss of fluorescence intensity over the full working range permissible with the objective (~200 μm)[64]. The results of the current study, however, observed a 50% reduction in fluorescence intensity within 100 μm when using a 20x dry objective. The difference in these observations is possibly the result of different equipment. One potential factor is the use of a higher-magnitude dry objective, when CUBIC-cleared samples (including CSAC-cleared samples) have an adjusted refractive index (RI=1.52) far closer to that of traditional immersion oil (RI=1.51) versus air (RI=1.00). Given that both CUBIC- and CSAC-cleared samples were compared on the same imaging platform in identical conditions, comparisons across the two protocols is still applicable in this case.

The 2-fold greater depth at which CSAC-cleared FluoSphere-embedded samples maintained at least 50% relative fluorescence intensity versus CUBIC-cleared samples suggests that the minor changes in the CSAC protocol produce a marked improvement in tissue clarity. Of particular note

is the introduction of a perfused bleaching solution to rapidly eliminate iron-containing chromophores, which have been shown to absorb light and impair fluorescence microscopy in thick tissue sections[58]. The follow-up perfusion with a diluted CUBIC-I reagent, as well, results in a delipidation process that can occur throughout the entire tissue volume at once, rather than only proceeding from the epicardial and endocardial surfaces. The far shorter incubation period necessary in CSAC-cleared samples is likely the result of this additional step.

While the FluoSphere-derived fluorescence was a useful metric in determining the impacts of absorption and light scattering on the loss of signal intensity, further studies must also incorporate additional fluorophores, which may require extended incubation periods. Hoechst 33342, a nuclear dye, was used as a control due to the expected uniform presence of nuclei in hearts harvested from healthy C57Bl/6J mice. The implementation of an area-controlled intensity metric considers the assumption of uniform nuclei density in the tissue sample, providing equal weight to both the brightness and number of nuclei detected. This, combined with local normalization and automated thresholding, should provide the most complete analysis of fluorescence reduction due to both dye penetration and light scattering and absorption.

The failure of SUT-cleared samples in the case of nuclei staining suggests an incompatibility with the stains used and the SUT reagent for clearing. As published results have suggested that SUT can reduce fluorescence with prolonged incubation times, it is possible that nuclear fluorescence was impacted. The formation of the hydrogel matrix may also have negatively impacted the penetration of the Hoechst dye into the tissue samples, which would be a negative indicator for the use of SUT for histological processing with the available equipment. The lack of ability to perfuse VA044 in PBS while degassing could have negatively impacted the formation of the hydrogel

matrix as well, leading to the observed degradation of the tissue, but this again suggests that the relative simplicity of the CUBIC and CSAC protocols are a significant advantage.

Comparing the nuclei-staining results in CSAC and CUBIC-cleared tissue, the fluorescence retention in CSAC-cleared tissue is far more apparent. The use of area-controlled fluorescence will result in more rapid loss of brightness compared to reporting of only mean intensity based on automated thresholding methods, so comparison of the reported decay rates compared to protocol results which report only mean fluorescence intensity in ROIs is disingenuous. Rather, direct comparison of number of nuclei detected (approximated through total nuclear area) and their brightness across samples processed in identical conditions will be more informative. In this study, the far greater retention of fluorescence in CSAC-cleared tissue samples against CUBIC-cleared samples under similar conditions is of note.

Conclusions

Based on the difficulty of implementing the SUT protocol with available equipment, length incubation times, and incompatibility with nuclei staining in its current implementation for established laboratory protocols, the SUT protocol was determined to be of lowest priority to pursue compared to both CUBIC and CSAC. While the additional perfusion steps taken as part of the CSAC protocol result in lengthier tissue extraction processes and require the use of specialized fixed-rate perfusion systems and multiple serial perfusions, the benefits of the protocol were considered to outweigh these additional costs. In particular, the potential for imaging along the full working distance of the available LSCM platform (tested at 0.3mm based on the potential for collision between the objective lens and microscopy cover glass) would result in a notable reduction in the number of physical slides necessary for preparation.

Study Limitations and Potential Extensions

The use of LSCM as the primary endpoint measurement, in particular with a dry objective, is a notable limitation of the study, which may result in underestimation of the actual transparency of CSAC-cleared cardiac sections. Further investigation, using perfused FluoSpheres and Hoechst 33342 in unison with LSFM, would be expected to produce results more in line with those typically reported by tissue-clearing protocols. Additionally, quantification of the permeability and compatibility of CSAC-cleared sections to antibody-based staining protocols would be an essential next step to properly prepare staining steps during sample preparation, in particular to establish ideal concentration ranges for antibodies of choice.

CHAPTER IV. THE IMPACT OF CELL-TYPE SPECIFIC INOS EXPRESSION ON POST-MI LEFT VENTRICULAR REMODELING AND FUNCTION

These CMR and histological techniques were then utilized in the analysis of post-MI remodeling and recovery of the myocardium when treated with cell-targeted interventions. Replacement of viable myocardium with collagen-rich infarct during remodeling also results in significant changes to the biomechanical properties of the heart, leading to the development of cardiomyopathies[68]. These biomechanical changes are correlated with changes in regional function, in particular radial and circumferential strain, which can be measured using non-invasive techniques such as Displacement Encoding with Stimulated Echoes (DENSE) CMR[69]. Global longitudinal strain (GLS) has been previously established as a potent feature for prediction of post-MI mortality alongside LVESV and LVEF[70]. Global circumferential strain has been compared with GLS for predictive capability[71,72], but regional circumferential strain perhaps serves an even greater predictive capacity for regional recovery of myocardium after MI[73,74].

The immune response after myocardial injury plays a key role in cardiac repair and long-term remodeling. The development of mature scar following myocardial infarction is the result of a complex interaction between inflammatory cells and cytokines, endothelial cells, myofibroblasts, and vascularization[75]. The traditional view of the timeline of injury following myocardial ischemia-reperfusion injury splits the response into distinct phases: inflammatory, proliferative, reparative, and maturation[76]. In each phase, cell populations are found to have elevated presence and activity within the different regions of the post-MI heart, with particular focus given towards infarct and border regions.

During the immediate response to reperfusion, widespread cytokine signaling by tissue-resident macrophages triggers infiltration of neutrophils into the infarct zone following reperfusion of the myocardium, where they begin clearing necrotic cardiomyocytes and cellular debris[77]. Following

the removal of tissue debris and as neutrophils begin to undergo apoptosis, fibroblasts undergo widespread proliferation and begin deposition of granulation tissue, the structure of which can impact long-term scar formation[78]. The reparative phase, which takes place once neutrophil populations within the infarct have been almost completely removed and the inflammatory response concludes, is considered within the specific context of transition of macrophages to alternative pro-reparative phenotypes, which will be described in more detail briefly as a critical consideration of this study. The final stage of the injury response involves the evolution and maturation of the collagen-rich scar and reduction of the presence of inflammatory cell types[79].

The inflammatory phase involves infiltration of $Ly6C^{hi}$ circulatory monocyte, which differentiate into pro-inflammatory macrophage phenotypes expressing CD68 and iNOS[80]. The reparative phase is marked by the transition of these pro-inflammatory, M1-like macrophage populations into reparative $Ly6C^{lo}$ macrophages, which can be identified by expression of CD206 and reduced expression of iNOS[81,82]. Concentration of CD206+ M2-like macrophage populations has been shown to peak during the late proliferative and early reparative phases of post-MI injury response[83]. These reparative macrophage subpopulations promote fibroblast proliferation and differentiation into myofibroblasts, generating massive amounts of ECM protein deposition, which eventually leads to the formation of mature scar as fibroblasts undergo apoptosis in late stages of recovery[84]. In summary, the inflammatory response that initially follows reperfusion results in a signaling cascade that activates myofibroblasts, leading to the eventual formation of scar in the myocardium, and broad modulation of this inflammatory response has been shown to improve cardiac function and reduce scar extent in post-MI recovery[85,86].

Complementary to the impact of the cellular inflammatory response on post-MI remodeling and scar formation, the presence of reactive oxygen species (ROS) in the infarct acts as a modulating

factor on cellular response. One of the most prominent drivers of excess ROS is the nitric oxide synthase (NOS) family of enzymes, neuronal NOS (nNOS), endothelial NOS (eNOS), and inducible NOS (iNOS)[87]. Under normal physiologic conditions, eNOS is constitutively expressed in endothelial cells and cardiomyocytes and produces low levels of nitric oxide, which is generally cardioprotective at low concentrations[88,89]. Unlike eNOS and nNOS, iNOS is not constitutively expressed in the myocardium, but its expression can be induced in both infiltrating macrophages, cardiomyocytes, cardiac fibroblasts, and endothelial cells by cytokines associated with inflammatory response[90–95].

Unlike eNOS and nNOS, iNOS expression of NO is a calcium-independent process, which can result in exceedingly high concentrations of NO output within short periods of time[96]. The high-output nature of NO expression by iNOS results in widespread elevation of NO concentration throughout the post-MI heart, which leads to cardiomyocyte death, elevated cytokine and inflammatory response, and reduced contractile function, though the nature of these effects at the molecular level is not well-explored[97–99]. Previously, our lab has shown that global knockdown of iNOS expression has resulted in reduced LV remodeling, greater retention of LV function, and reduction of circumferential wall thinning in mouse models of ischemia-reperfusion injury[100]. This study is intended to investigate the contributions of iNOS expression in different cell populations on these observed therapeutic effects. Expression of iNOS in cardiomyocytes and macrophages will be investigated using cell type-specific Cre expression vectors to eliminate iNOS expression.

Methods

The animal protocol used in this study was approved by the University of Virginia Animal Care and Use Committee (Protocol 2802) and conformed to the Guide for the Care and Use of Laboratory Animals (ILAR; Revised 2011).

TRANSGENIC MOUSE MODEL OF MACROPHAGE-SPECIFIC INOS KNOCKOUT

Transgenic macrophage iNOS knockout (MΦ-iNOS-KO) mice were generated on a C57BL/6 background by crossing mice homozygous for floxed iNOS (Gift from the laboratory of André Marette at Laval University, Quebec City, Canada) with hemizygous LysM-Cre[101] resulting in macrophage-specific Cre expression for macrophage-specific iNOS knockout. Figure 12 presents a simple graphic which shows the particular knock-in genes of interest in the resulting crossed mouse. While LysM-Cre is a knock-in model to induce Cre expression in macrophages, it is important to note that there is a potential to drive Cre expression in up to 70% of neutrophils as well, which could additionally contribute to iNOS expression in the early inflammatory stages of post-MI injury response[102]. To minimize mortality due to complications following surgery to induce myocardial infarction, mice were selected to fall within a weight range of 20-28 grams body weight on the day of infarction.

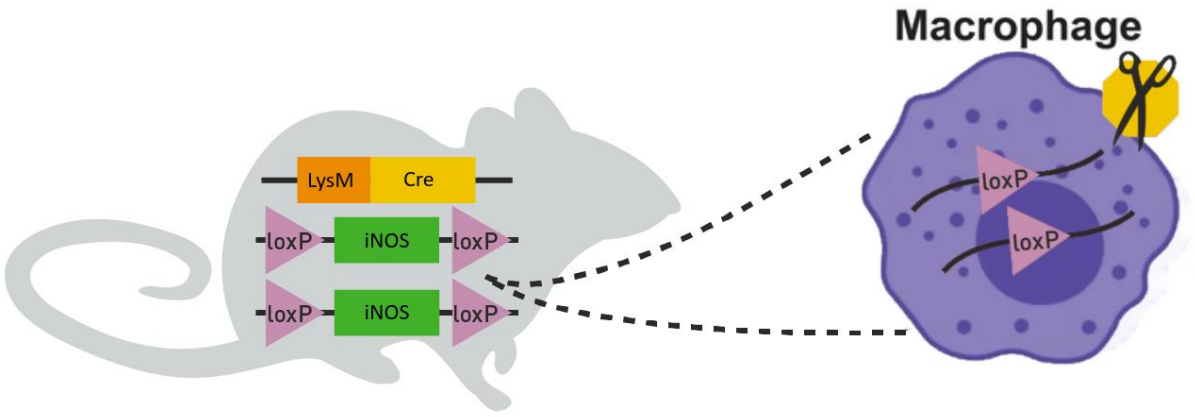

Figure 12. LysM-Cre mediated iNOS Knockout Mouse Model. Mice hemizygous for Cre expression on the LysM gene produced Cre in macrophages and neutrophils. Crossed with a transgenic loxP-flanked (floxed) iNOS allele, this results in a transgenic knockout of iNOS expression within the affected cell types.

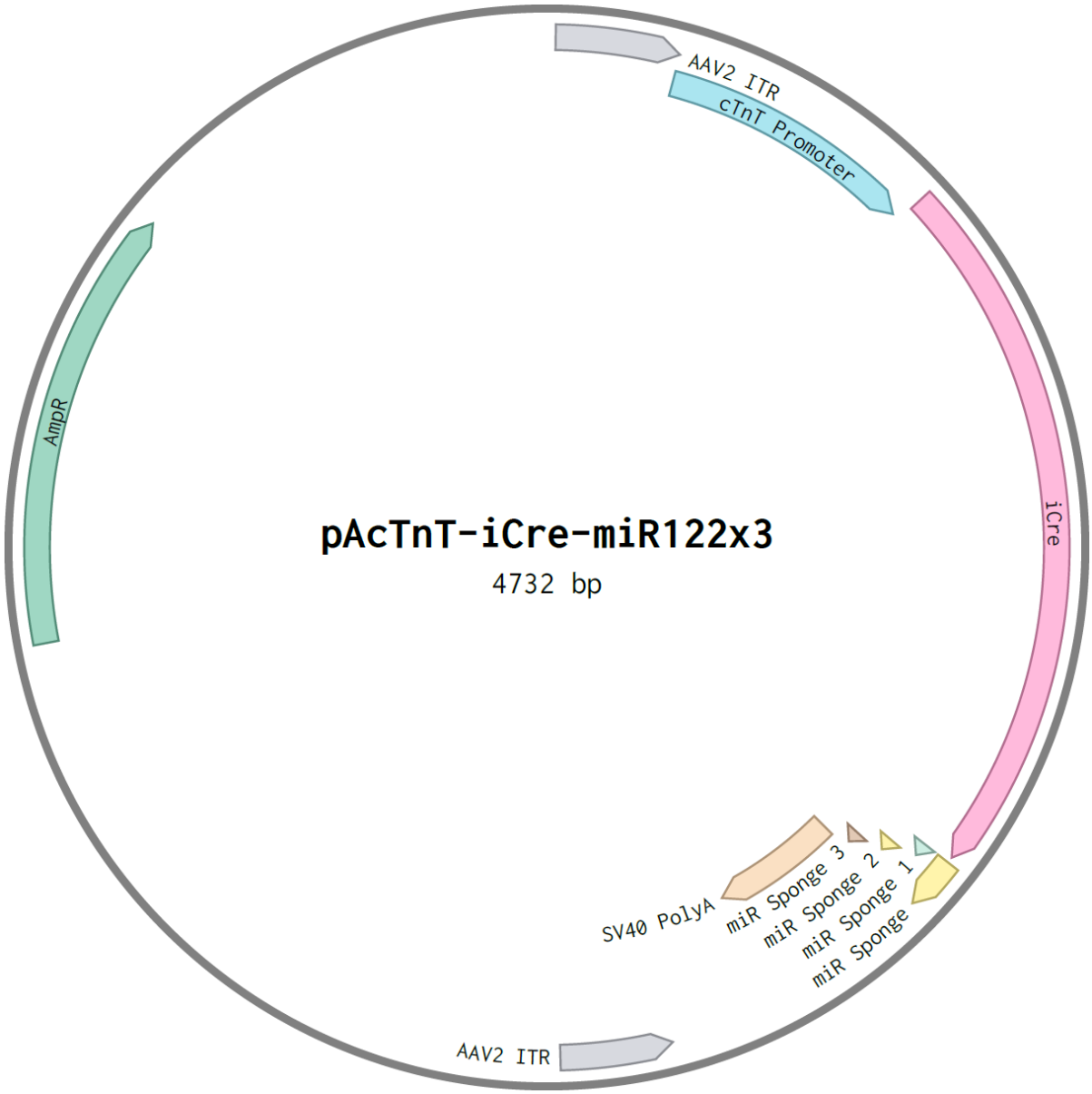

Figure 13. AAV Driving Cardiomyocyte-Specific Cre Expression. The AAV plasmid sequence used to produce AAV9 for cardiomyocyte-specific induction of Cre expression. The included miR sponge sequences are included to reduce transgene expression in the liver. The cTnT promoter used produces highly specific expression in cardiomyocytes.

AAV-INDUCED CARDIOMYOCYTE-SPECIFIC INOS KNOCKOUT

Cardiomyocyte-specific Cre expression was initiated using AAV9 driving Cre expression using the cardiomyocyte-specific cTnT promoter[103]. The AAV additionally contained 3 repeated sequences for microRNA-122, indicated on the sequence map, to inhibit transgene expression in the liver. The AAV sequence used for cardiomyocyte-specific Cre expression is shown in Figure 13. AAV used for the study was produced and packaged by Origene (Rockville, MD) using their triple-transfection protocol. AAV was delivered to mice 2 weeks prior to the induction of MI at a dose of 2e13 vp/kg b.w. from a stock concentration of 6e12 vp/ml, delivered via intravenous injection through the mouse tail vein. Injections were performed in mice containing the floxed iNOS gene, resulting in cardiomyocyte-specific iNOS knockout (CM-iNOS-KO).

MOUSE MODELS OF REPERFUSED MYOCARDIAL INFARCTION

In total, 23 MΦ-iNOS-KO (Jackson Labs, Bar Harbor, ME), 19 CM-iNOS-KO, and 17 floxed iNOS mice underwent surgery to induce MI.

Our lab has previously established the utility of a murine model of transient LAD occlusion for investigation of post-MI outcomes in reperfused MI[104]. Prior to induction of myocardial infarction, mice were anesthetized using a mouse anesthetic cocktail containing 60 mg/kg b.w. ketamine and 5 mg/kg b.w. xylazine via intraperitoneal injection. Mice were orally intubated to maintain artificial respiration using a rodent ventilator with an FiO_2 of 0.80, frequency of 100 strokes/minute, and tidal volume of 10 ml/kg. Mouse body temperature is monitored using a thermocouple thermometer and maintained at 37 +/- 0.5 C with a heat lamp. The left pleural cavity is approached by cutting the left third and fourth ribs using a cautery pen and the intercostal muscles using scissors to expose the heart. A 7-0 silk suture is passed beneath the LAD at the level of the lower atrium and is tied down over a segment of PE-50 tubing to occlude the LAD. ECG

changes and blanching of the risk region confirm successful occlusion and induction of MI. Occlusion is maintained for 1 hour prior to removal of the suture and tubing to achieve reperfusion. The incision site is sealed using nylon sutures and the mice are provided with local injections of bupivacaine around the incision as an analgesic, following dosage guidelines provided with the medication. Induction of ischemia was performed by a member of the lab trained in survival surgical techniques for myocardial infarction, Dr. Lanlin Chen.

CMR ANALYSIS OF POST-MI LV REMODELING AND FUNCTION

Assessment of myocardial function was performed on a 7T ClinScan MRI system (Bruker; Billerica, MA), using a 4-channel cardiac surface array coil. Mice were anesthetized using a vaporizer delivering 1.25% isoflurane in oxygen during all imaging procedures. Mouse vitals of heart rate, respiratory rate, and temperature were monitored during imaging using an ERT Control/Gating Module (SA Instruments, Inc; Stony Brook, NY). Mouse body temperature was maintained at 36.5+/-0.5C for the duration of imaging using circulating heated water. To minimize artifacts, all imaging sequences used for analysis were performed with gating for respiratory motion. For sequences involving gadolinium enhancement, a catheter was inserted in the peritoneum of the mouse for delivery without the need to remove the mouse from the scanner. Imaging protocols were performed 2 days prior to induction of myocardial infarction to assess

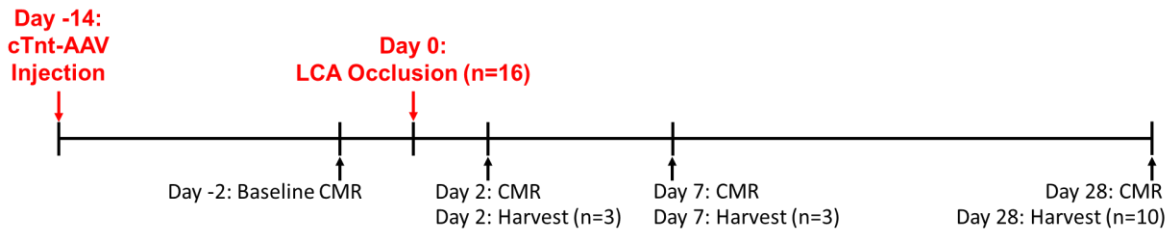

Figure 14. Per-Group Study Timeline. Proposed timeline of CMR and histology endpoints. AAV injection was only performed in CM-iNOS-KO mice, at 14 days prior to induction of MI. CMR after MI included long-axis black-blood, full-heart short-axis cine black-blood and LGE, and short-axis DENSE at 3 mid-ventricular slices. LGE was not performed at baseline.

baseline values, and then again at 2, 7, and 28 days following MI. A timeline of procedures, including CMR and histology endpoints and desired group size, is shown in Figure 14.

Localizer images were performed first to identify long-axis and mid-ventricular short-axis slices. Following localization, the MRI protocol included collection of black-blood cine images oriented in the long-axis, 4-chamber, and short-axis views of the heart. Short-axis images were captured using a 1mm slice thickness with no gaps, ranging from the base to the apex of the heart. DENSE images for cardiac strain assessment were captured in the same image position as the three short-axis BB images nearest to the mid-ventricle height. A solution containing gadolinium was delivered after DENSE imaging, dosed to 0.6 mmol/kg body weight of the mouse. LGE MR was initiated 10 minutes after gadolinium was delivered, using the same slice positions that were used for BB short axis imaging.

Cine black-blood and LGE images were processed using Segment Research (Medviso; Lund, Sweden). Endocardial and epicardial contours at end-diastole and end-systole were manually traced and pinpoints were placed to denote RV insertion points. Additional pinpoints were placed using the long-axis black-blood images to denote the base-apex orientation of the image stack. Endocardial and epicardial contours were traced in the LGE image stack and scar was delineated manually using Segment Research. Values for left-ventricular end-diastole and end-systole volumes, left-ventricular mass, ejection fraction, and infarct size as a percentage of LV mass were identified from these images. Regional wall thickness was performed using a 12-sector model, which were separated evenly by angular rotation around the center point of the endocardial contour in each slice. Sectors were manually aligned using RV insertion point placement, and assigned a status of infarct, border, or remote based on LGE-based infarct segmentation. Infarct sectors were defined as sectors with >50% infarct presence by area, while border sectors were any non-infarct

sectors which were adjacent to infarct sectors, either circumferentially or longitudinally, and remote sectors were all non-infarct, non-border sectors.

DENSE images were analyzed using the DENSEanalysis package for MATLAB[37,38]. Endocardial and epicardial contours were manually traced in each slice and timepoint prior to phase unwrapping and strain calculation using the built-in techniques as part of the software. Strains calculated from 2D DENSE images were then exported for each slice.

AUTOMATED CO-REGISTRATION OF CMR USING COCATOO

Data gathered from each analysis pipeline were then imported into CoCaToo using a custom processing script. For the model alignment method, the finite-element model was instantiated with 28 elements from base to apex, 5 elements from endocardial to epicardial surface, and 48 elements spanning the rotation around the long axis, for a total of 6720 elements in the full model. This mesh density represented a balance between processing speed, memory footprint, and maintaining the resolution of the input data as best as possible. As mentioned previously, elements were only used for calculations if strain values could be interpolated for that element, and elements were otherwise ignored for all model-derived values. Complete analysis was performed at multiple border zone widths due to difficulty in identifying an objective metric to determine border zone size in individual subjects. Data is reported as mean ± SEM.

To validate results from CoCaToo automated processing methods, established lab practices for CMR processing were performed. Using the previously mentioned LGE-based sector assignments and 6 equiangular sectors in DENSE-derived images (limited due to software limitations), sector-by-sector peak strains were calculated. DENSE-derived circumferential strains were calculated for each subject and averaged based on sector classification, treatment status, and timepoint post-MI. Data is reported as mean ± SEM.

IMMUNOHISTOCHEMICAL METHODS IN POST-MI HEARTS

Mice were sacrificed for harvesting of hearts following completion of imaging. The majority of mice were sacrificed after imaging on day 28, while additional mice were sacrificed at earlier timepoints for histological assessment. Mice were anesthetized using a mouse anesthetic cocktail containing 60 mg/kg ketamine and 5 mg/kg xylazine delivered via intraperitoneal injection. Once mice were confirmed to be nonresponsive to external stimulus, the abdominal cavity was opened, and death was confirmed by bilateral thoracotomy. Prior to harvesting of the hearts, a catheter was inserted into the apex of the left ventricle for perfusion of the heart according to the CSAC protocol, with slight modifications. Modifications made involved the slicing of tissue samples prior to IHC and refractive index matching techniques. While these procedures can introduce greater challenge with alignment of resulting confocal images, incubation times and quantity of antibody needed for tissue staining were reduced significantly.

Hearts were perfused with 30 ml of PBS containing 4% paraformaldehyde and 500 USP units of heparin over a period of 20 minutes. Hearts were then perfused with 30 ml of bleaching solution comprising 7.5% hydrogen peroxide and 25% ethanol in water for 20 minutes. A final perfusion of 30 ml 25% CUBIC-I in water was perfused over 20 minutes again before the hearts were removed. Hearts were incubated in CUBIC-I on a rocker until optically transparent based on visual observation. At this stage, hearts were mounted onto a syringe mount for a CompressTome slicer (Precisionary Instruments; Natick, MA), embedded in 2% agarose, and sliced at 250 μm thickness, beginning at the apex. Slices were transferred to a 48-well tissue clean culture plate with positional information and slice orientation recorded to begin antibody staining for immunolabeling of desired biomarkers.

The immunofluorescence protocol used was designed to evaluate cell types and iNOS expression in the cleared cardiac slices. Primary antibodies and dilutions for staining were a monoclonal rat anti-CD68 (1:200), polyclonal goat anti-CD206 (1:200), polyclonal rabbit anti-iNOS (1:50), and AlexaFluor-647 preconjugated mouse anti-cardiac troponin T (cTnT) (1:50) (All ThermoFisher; Waltham, MA). Samples were incubated in non-fluorescent primary antibodies in 1% Triton X-100 in PBS for 48 hours on an orbital shaker at room temperature, then underwent four successive 15-minute wash cycles using 1% Triton X-100 in PBS and a final overnight wash step in 1% Triton X-100 in PBS. AlexaFluor Plus 405-conjugated anti-Rabbit (1:200), AlexaFluor Plus 488-conjugated anti-Goat (1:200), and AlexaFluor Plus 555-conjugated anti-Rat (1:200) secondary antibodies all raised in donkey (All ThermoFisher; Waltham, MA), along with the AlexaFluor 647-conjugated anti-cTnT, were added to samples in 1% Triton X-100 and incubated for 48 hours at room temperature on an orbital shaker. Samples were then washed for four cycles of 15 minutes in 1% Triton X-100 in PBS and transferred into CUBIC-II overnight for refractive index matching.

Samples were removed from CUBIC-II and mounted on microscopy slides featuring a 250 μm spacer made of high-temperature PTFE surrounding a small circular well for sample placement. CUBIC-II was added to until samples were completely immersed with no bubbles and covered using #1 micro cover glass (VWR; Radnor, PA) before sealing with nail polish. Samples were imaged on a Leica Stellaris 5 upright confocal microscope using a 20x dry objective. Z-stack slices were obtained starting at the surface of the sample and continuing at every 50 μm. Slices were stitched using the automated stitching tools available in the imaging software and exported as full-resolution TIF image files for analysis.

COCATOO PROCESSING OF FLUORESCENCE MICROSCOPY IMAGES

Confocal microscopy images were imported into CoCaToo for manual segmentation and assessment. Images containing high levels of tissue deformation, either due to tearing, folding, or warping of the left ventricle, were excluded for automated processing methods. Image slice positions were recorded based on recorded slice numbering when initial mechanical slicing was performed, with slight additional offsets due to z-position depth for the slice during imaging. Slices were confirmed for proper orientation, and image stacks were mirrored in cases of inverted orientation relative to CMR images. Endocardial and epicardial surfaces were manually traced in slices with sufficiently high image quality, determined by a visual assessment for clearly defined myocardium, lack of imaging artifacts or obstructions, and clearly defined positions for RV insertion points into the LV. Positions and contours were saved and data files were exported for each slice to use for automated alignment and processing with the common cardiac model.

Histological results were also assessed manually to qualitatively assess CoCaToo-based automated fluorescence processing.

STATISTICAL METHODS

Data are presented as mean ± SEM. Comparisons between groups were assessed using a Linear Mixed Model with Random Effects, performed in SPSS (IBM Corp. Released 2021. IBM SPSS Statistics for Windows, Version 28.0. Armonk, NY: IBM Corp). Linear regression was performed using treatment and timepoint as fixed effects, baseline volume as a covariate effect to control for inter-subject variability in baseline volumes, and subject ID for introduction of random effects. Pairwise comparisons between groups were performed using estimated marginal means with a Bonferroni correction factor for multiple comparisons[105].

Results

INFARCT SIZE AND MORTALITY

Infarct sizes at day 2 post-MI as assessed by LGE were similar across groups (Control: 48.8 ± 1.9 % LVM, MP-iNOS-KO: 44.6 ± 2.0 % LVM, CM-iNOS-KO: 47.3 ± 3.6 % LVM; p = NS). Mortality following surgical induction of ischemia was high: 13 MΦ-iNOS-KO, 11 CM-iNOS-KO, and 3 floxed iNOS mice died prior to completion of imaging on day 2. MΦ-iNOS-KO and CM-iNOS-KO mortality rates helped inform animal sizes to improve survival after MI, which resulted in far lower mortality in the control group. Post-mortem autopsies were performed to check for potential causes of death. No mice exhibited ventricular rupture or internal bleeding, suggesting that mortality was the result of sudden cardiac death following MI induction, likely through development of cardiac arrhythmias[106].

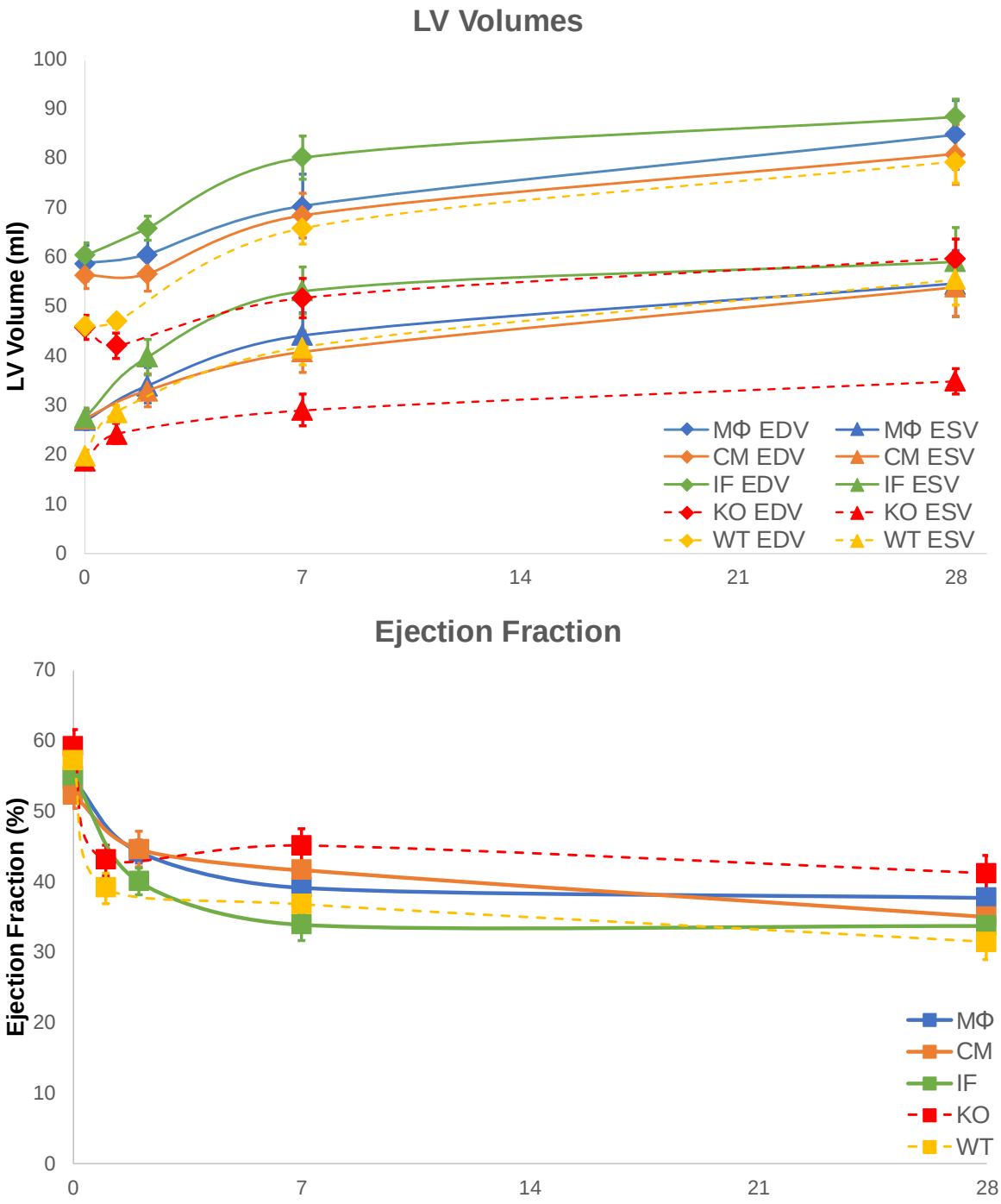

Figure 15. Timeline of LV Remodeling. Changes in LV Volumes following induction of MI followed expected trends. Treatment groups exhibited slower progression of adverse remodeling, but failed to result in a significant cardioprotective outcome. Change in ejection fraction mirrored changes in EDV and ESV, with the greatest impact of either therapeutic at 7 days post-MI, but no observed long-term efficacy. A comparison to previously-observed effects from global iNOS knockout (KO) is presented, alongside wild-type (WT) controls. Using linear mixed models controlling for inter-subject variability in baseline volumes, no significant difference is observed.

LEFT VENTRICULAR VOLUMES AND EJECTION FRACTION

A comparison of the changes in end-diastolic and end-systolic LV volumes in cell type-specific iNOS knockout mice following MI identifies trends that mirror those observed in global iNOS$^{-/-}$ mice, but to a lesser degree of impact[100]. EDV, ESV, and EF trends for each study group are presented in Figure 15. ESV is similar at baseline across all groups (Control: 27.7 ± 1.9 μl; MP-iNOS-KO: 27.1 ± 1.9 μl; CM-iNOS-KO: 27.4 ± 2.0 μl; p = NS). At day 2 post-MI, both treatment groups trend towards lower increases in value, but do not differ significantly from the control group (Control: 39.9 ± 3.6 μl; MP-iNOS-KO: 34.1 ± 3.6 μl; CM-iNOS-KO: 33.1 ± 3.3 μl; p = NS). At day 7 post-MI, the greatest separation between group means is observed, but results are still not statistically significant (Control: 53.2 ± 4.8 μl; MP-iNOS-KO: 44.3 ± 4.5 μl; CM-iNOS-KO: 40.9 ± 4.1 μl; p = NS). By day 28, the difference between group means is reduced, and knockout models present similar results to control mice (Control: 53.2 ± 4.8 μl; MP-iNOS-KO: 44.3 ± 4.5 μl; CM-iNOS-KO: 40.9 ± 4.1 μl; p = NS).

An assessment of EDV shows similar results to observations from ESV. Baseline EDV across groups show little to no difference (Control: 60.5 ± 2.6 μl; MP-iNOS-KO: 58.9 ± 3.5 μl; CM-iNOS-KO: 56.5 ± 2.8 μl). Changes in EDV by day 2 post-MI are minor, with no groups exhibiting significant differences relative to baseline (Control: 66.0 ± 2.4 μl; MP-iNOS-KO: 60.6 ± 4.8 μl; CM-iNOS-KO: 56.8 ± 3.7 μl; p = NS). By day 7, control mice have significantly elevated EDV relative to baseline (80.3 +/- 4.4 μl; $p<0.001$), while both knockout groups trend closer to baseline results (MP-iNOS-KO: 70.5 ± 6.5 μl; CM-iNOS-KO: 68.6 ± 4.5 μl). A comparison between group means at day 7 however, does not establish any significant difference between either treatment group versus control. At day 28, the difference between group means has largely diminished as treatment groups have developed significant increases in EDV versus baseline values (Control: 88.6 ± 3.5 μl; MP-iNOS-KO: 84.9 ± 7.1 μl; CM-iNOS-KO: 81.0 ± 6.1 μl).

Comparing EF presents similar findings to EDV and ESV in both control and treatment groups. The largest difference between group means is observed on day 7 post-MI, as EF in control mice has reduced by ~40% relative to baseline values, versus a 29% and 21% reduction observed in MP-iNOS-KO and CM-iNOS-KO groups, respectively.

REGIONAL WALL THINNING

Assessment of wall thickness shows prominent differences across groups based on regional classification. Absolute wall thickness is shown in Figure 16, presented in mm ± SEM.

In all groups, there is an initial swelling of the infarct region at day 2, which is most pronounced in CM-iNOS-KO mice, followed by MP-iNOS-KO and then control (Control: 0.87 ± 0.03 mm; MP-iNOS-KO: 0.96 ± 0.04 mm; CM-iNOS-KO: 1.05 ± 0.03 mm; CM vs Control $p < 0.01$). By day 7, the infarct wall has begun to undergo notable thinning in both control and MP-iNOS-KO mice, while the infarct wall has returned to similar thickness relative to baseline in CM-iNOS-KO mice and is significantly thicker than both MP-iNOS-KO and control groups ($p<0.05$). Both treatment groups exhibit significantly less thinning than control mice by this stage. By day 28, all treatment groups exhibit prominent wall thinning in the infarct, though CM-iNOS-KO is still significantly less thin than controls (Control: 0.62 ± 0.02 mm, CM-iNOS-KO: 0.71 ± 0.02 mm; $p = 0.02$), while MP-iNOS-KO exhibit similar results to control mice.

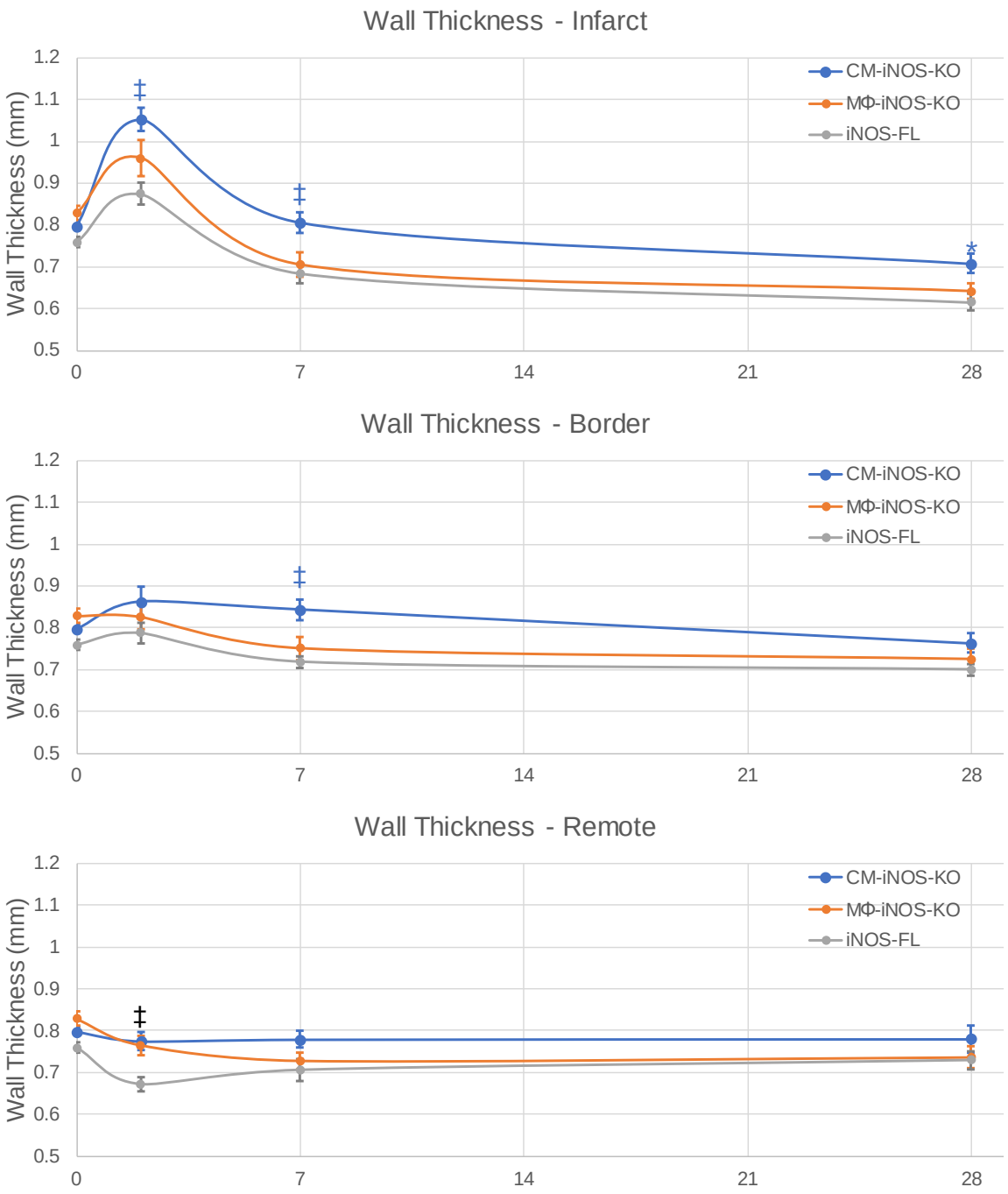

Figure 16. Comparison of Regional Wall Thickness. Cardiomyocyte-specific iNOS knockouts presented significantly elevated infarct wall thickness relative to control mice, as well as border zone wall thickness at day 7 post-MI. Control mice additionally exhibited significant wall thinning in the remote region at day 2 post-MI relative to both treatment groups. (‡ = $p < 0.01$; * = $p < 0.05$; Blue symbols indicate CM-iNOS-KO comparison to baseline).

Border regions in MP-iNOS-KO are relatively unaltered by day 2 post-MI, while both control and CM-iNOS-KO experience mild swelling, though of far lower magnitude than the changes observed in the infarct region. At day 7, border zones in CM-iNOS-KO mice remain slightly thicker than baseline, while both MP-iNOS-KO and control mice have thinned slightly relative to baseline. Border regions in all groups are thinner than baseline at day 28 post-MI, with CM-iNOS-KO mice experiencing significantly less thinning than control mice.

Wall thickness in the remote sectors is relatively unchanged in both treatment groups at day 2, while thinning is observed in control mice (CM: $p<0.01$; MP: $p<0.01$). This thinning is partially recovered by day 7, while both treatment groups begin to undergo very mild thinning versus baseline, resulting in similar values across groups. Differences between days 7 and 28 post-MI in the remote regions are minor, with mild thinning observed in each group, to a far lower extent than is observed in the infarct region.

REGIONAL CIRCUMFERENTIAL STRAIN BY MANUAL ALIGNMENT

Reported strain values are based on the peak circumferential strain (E_{cc}) identified during the cardiac cycle, as measured with DENSE. Higher-magnitude strain values represent more significant shortening of the myocardium during contraction and greater retention of myocardial function in post-MI contexts.

At baseline, E_{cc} magnitudes across the sectors are similar, though the anteroseptal and inferoseptal sectors exhibit slightly lower magnitude than non-septal sectors. For the purpose of comparison, strain at baseline was averaged across all sectors and used as the initial strain in the remote, adjacent, and infarct regions, though no infarct segmentation was performed at this timepoint.

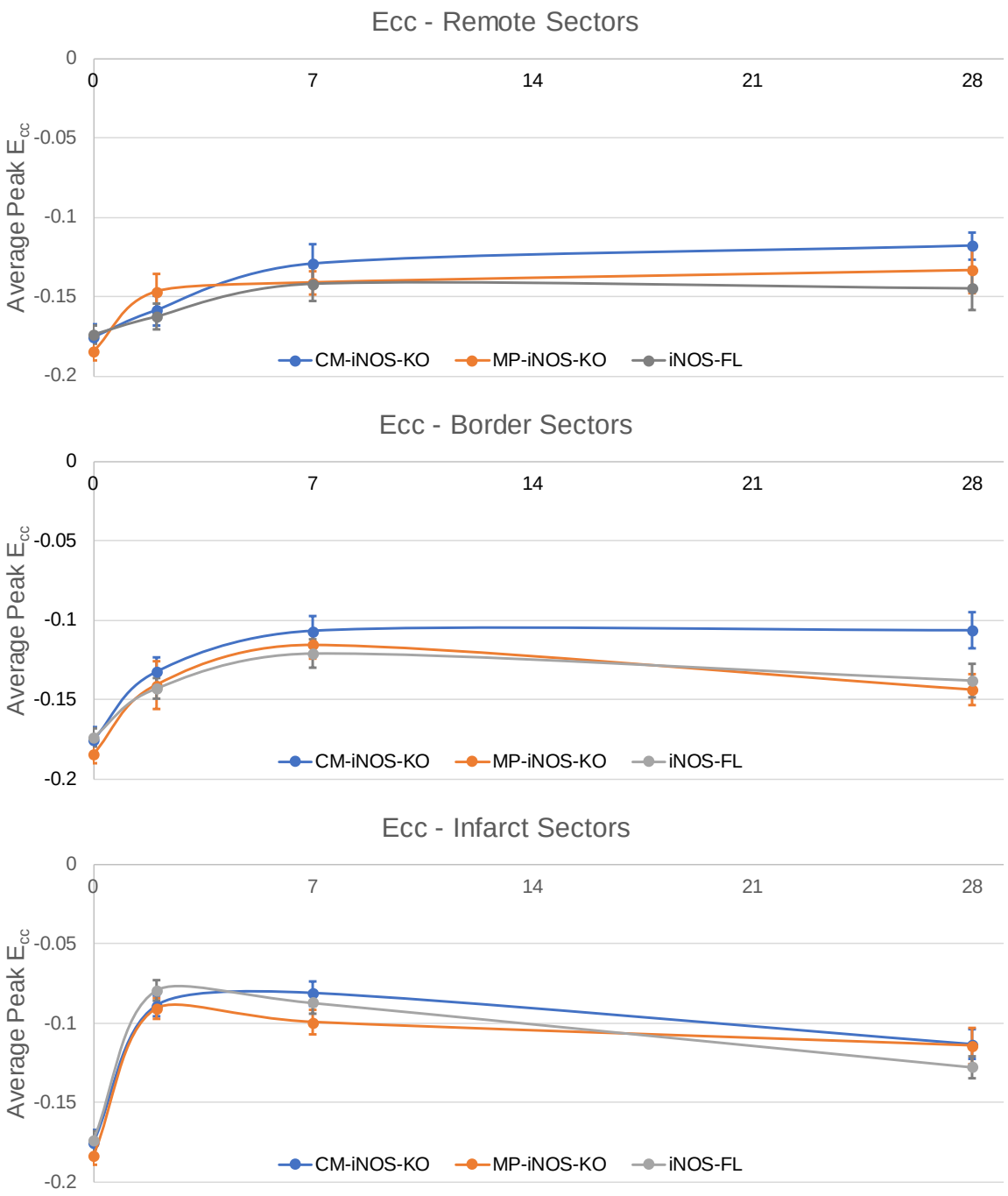

Figure 17. Comparison of Manually-Aligned Peak E_{cc}. Trends in circumferential strain suggest that the impacts of iNOS knockout in specific cell types does not significantly alter cardiac function after MI. Prior studies of global iNOS knockout mouse models have suggested that borderzone function may be transiently improved relative to controls, but this trend was not observed in cell type-specific knockout. Values from baseline CMR timepoints are indicated on graphs at timepoint 0.

Initial E_{cc} magnitudes were -0.175 ± 0.004 in CM-iNOS-KO, -0.185 ± 0.004 in MP-iNOS-KO, and -0.174 ± 0.004 in Control mice (p = NS).

On day 2 post-MI, maximal E_{cc} magnitudes in the infarct sectors are significantly diminished in the control group (-0.079 ± 0.006). Strains remained diminished by day 7 (-0.087 ± 0.007), with partial recovery by day 28 post-MI (-0.128 ± 0.007). Mice with cell-type specific iNOS knockouts generally had similar outcomes. At day 2 post-MI, the infarct region of CM-iNOS-KO mice exhibited similar peak strain relative to control (-0.089 ± 0.007). At day 7, strain in the infarct region remained weakened, and had weakened slightly relative to day 2 (-0.081 ± 0.008). However, by day 28 post-MI, infarct strains were exhibiting a similar trend in recovery compared to control mice (-0.113 ± 0.009). MP-iNOS-KO mice had similar results at day 2 post-MI versus both control and CM-iNOS-KO mice (-0.091 ± 0.007) with a similar trend of recovery compared to control mice at day 7 (-0.099 ± 0.008). At day 28, strains were similar to those in CM-iNOS-KO mice (-0.114 ± 0.011).

Border zone sectors similarly experienced significant impairment of strain at day 2 post-MI in all treatment groups (Control: -0.143 ± 0.006; MP-iNOS-KO: -0.141 ± 0.015; CM-iNOS-KO: -0.133 ± 0.009). By day 7, strains continued to worsen in both control and CM-iNOS-KO groups but remained similar in MP-iNOS-KO mice (Control: -0.121 ± 0.009; MP-iNOS-KO: -0.116 ± 0.008; CM-iNOS-KO: -0.107 ± 0.010). Slight recovery was observed in all groups by day 28 relative to day 7 peak strains (Control: -0.138 ± 0.010; MP-iNOS-KO: -0.144 ± 0.010; CM-iNOS-KO: -0.106 ± 0.011).

Comparing remote sector strains, MP-iNOS-KO mice had the highest magnitude shift in peak E_{cc} compared to baseline, but all groups had similar trends overall at day 2 (Control: -0.162 ± 0.008, MP-iNOS-KO: -0.147 ± 0.012, CM-iNOS-KO: -0.159 ± 0.009, p = NS). MP-iNOS-KO mice

exhibited minimal change from day 2 to day 7, while both control and CM-iNOS-KO mice showed reduced peak strains (Control: -0.142 ± 0.010, MP-iNOS-KO: -0.141 ± 0.008, CM-iNOS-KO: -0.129 ± 0.013). By day 28, no groups exhibited significant change relative to day 7, and showed no notable recovery back to baseline values (Control: -0.145 ± 0.013, MP-iNOS-KO: -0.133 ± 0.014, CM-iNOS-KO: -0.118 ± 0.009). Results of manual strain alignment are presented in Figure 17.

ASSESSMENT OF COCATOO-BASED STRAIN ANALYSIS

Model-derived strain trends were generally similar to those derived from manual sector-based analysis methods, though absolute strain magnitude did have differences. Strains based on CoCaToo automated alignment methods are presented in Figure 18. Strains within the infarct region exhibit the greatest similarity, with an average difference of only 3.8% across all groups and timepoints. In both border and remote regions, model-based coregistration results in slightly lower-magnitude strains across all groups and timepoints post-MI by approximately 20% in border and 12% in remote regions. As this was a generally universal adjustment, relationships between groups for comparison is generally unchanged. As in manual alignment, no significant differences were found between groups, suggesting that iNOS knockout from specific cell types is insufficient to cause large-magnitude changes in regional function post-MI.

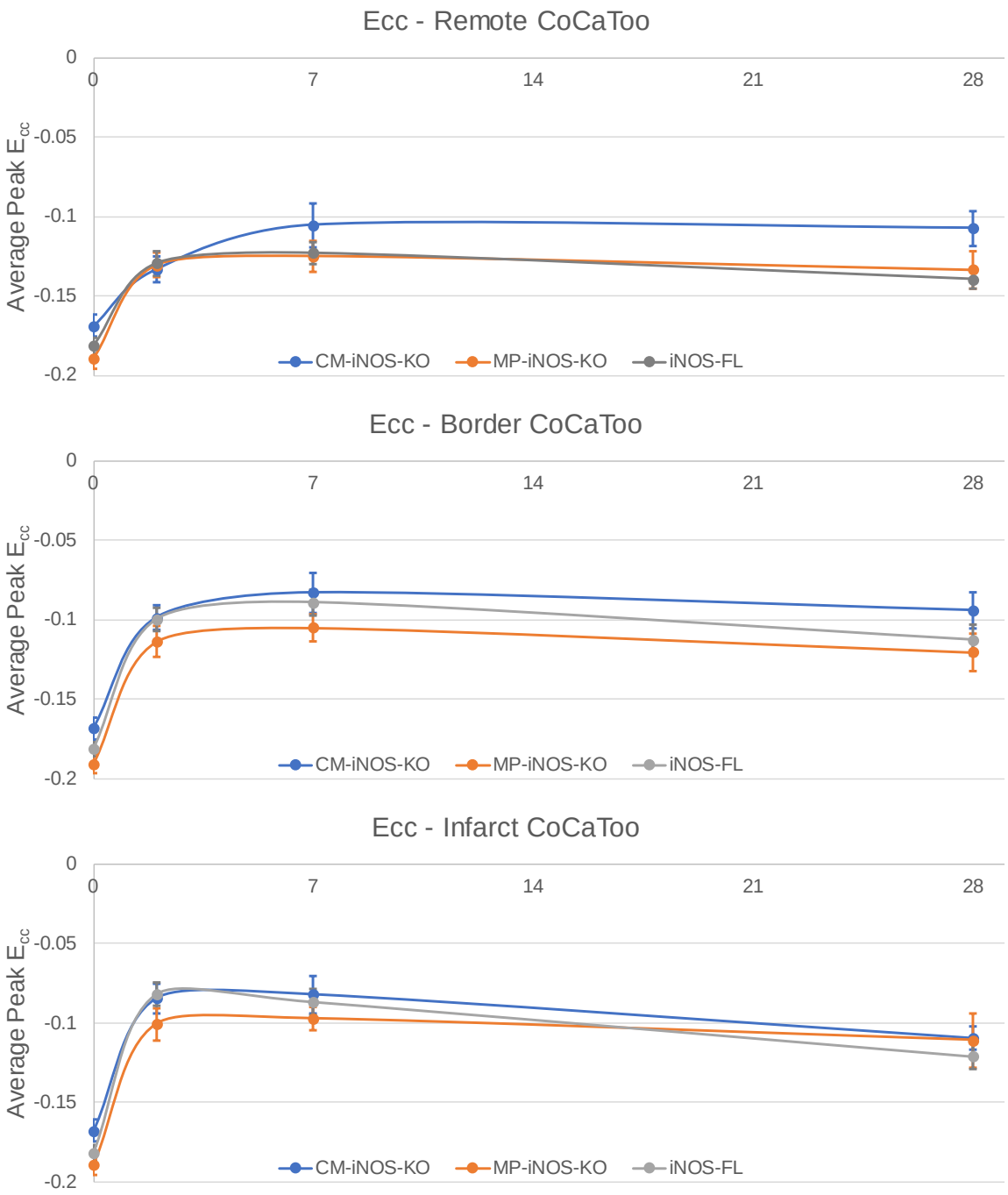

Figure 18. Comparison of Model-Aligned Peak E_{cc}. Model-based automated alignment presents similar results to manual alignment. Infarct alignment, which is based on strict delineation, shows the greatest similarity compared to manual alignment, while spatially-varying border and remote region results generally result in lower-magnitude strain values.

AUTOMATED CO-REGISTRATION OF FLUORESCENCE MICROSCOPY AND CMR

Multiple images were excluded from automated processing due to either tearing, severe warping, or folding of the myocardium, as such errors prevent proper contour segmentation and pinpoint placement. In total, 3 CM-iNOS-KO, 3 MP-iNOS-KO, and 2 iNOS-FL mice were used for contouring and model processing. As a result, while comparisons can identify potential trends, additional subjects would be necessary to consider statistical significance of presented findings. Raw export images were used for quantification to avoid introducing manual bias and to assess model quality with unmanipulated images.

Hearts from iNOS-FL mice were extracted at days 2 and 7 post-MI for histological assessment to provide context for the anticipated major influence of CM-iNOS-KO and MP-iNOS-KO on infarct formation and early LV remodeling. Histology performed in hearts extracted on day 28 post-MI was removed from automated assessment due to poor slice quality. In these subjects, automated coregistration identified a 15.2% and 38.8% fluorescence difference between infarct and remote regions in the 405nm channel at days 2 and 7, respectively, which is expected to represent similar increases in iNOS concentration. MP-iNOS-KO hearts extracted on day 2 post-MI exhibited a 4.7% difference, and a CM-iNOS-KO heart extracted on day 7 post-MI exhibited only a 3.8% difference. In border zone elements, the average fluorescence difference in control groups was only 12.5% and 12.9% on days 2 and 7.

Analysis in the 488nm channel represents presence of CD206-expressing macrophages. Control mice exhibited a 35.8% and 24.9% increase in infarct-region vs remote-region fluorescence based on model results at days 2 and 7, while border regions were elevated by 27.3% and 6.8%. Day 2 MP-iNOS-KO fluorescence results yielded inconsistent results across the two hearts: 18.7% lower fluorescence vs 25.0% higher fluorescence between the two samples relative to remote region

fluorescence. CM-iNOS-KO infarct fluorescence at day 7 was similar to remote, with a 4.5% lower fluorescence, while day 28 exhibited an average of 35.5% higher fluorescence in the infarct.

Results of processing in the 555 nm channel, used to label CD68 expression, showed similar results to that observed at 488 nm. Samples from control mice were 27.7% more fluorescent in the infarct at day 2 and 2.4% less fluorescent at day 7. MP-iNOS-KO mice had similar fluorescence in infarct and remote regions at day 2 (6.6% higher fluorescence) and at day 28 (3.0% reduced fluorescence). Day 7 CM-iNOS-KO results had elevated fluorescence in the infarct (22.7% increased fluorescence) which was retained by day 28 (27.7% increased fluorescence).

Model-based fluorescence in the 647nm channel is intended to represent viable cardiomyocyte presence, which should primarily indicate lack of infarct in areas of elevated fluorescence. However, only 2 of the 8 analyzed mice calculated a difference in remote and infarct-region fluorescence of more than 10%: a CM-iNOS-KO mouse heart extracted 28 days after MI and a control mouse heart extracted at day 2 post-MI. In both of these cases, an increase in infarct-region fluorescence versus remote regions was detected, while a decrease in fluorescence is anticipated in the infarct region.

MANUAL HISTOLOGICAL ANALYSIS OF THE POST-MI BORDER ZONE

Due to poor fitting results from model-based quantitative histological processing, manual review of histology was performed. Histological images are presented with CD68 and iNOS channels overlaid to view fine details in the border zone, due to relatively lower fluorescence in these channels relative to cTnT and CD206 staining. Histology taken from hearts extracted from control mice at day 2 post-MI is seen in Figure 19. CD68 and iNOS expression were found to colocalize near the border of the infarct region, while CD206-expressing macrophages are widespread

throughout the myocardium. In MP-iNOS-KO mice, CD206-expressing macrophages were observed in high density in the infarct region, while CD68 was more evenly distributed through the myocardium with minimal colocalization of iNOS expression, as seen in Figure 120.

Histological assessment at day 7 post-MI in hearts from control mice is shown in Figure 21. CD206-expressing macrophages are present in the infarct in high concentration, while expression of CD68 is observed more sparsely through the myocardium. iNOS expression is found in the infarct region, but not colocalized with CD68, suggesting a potential change in phenotype of remaining CD68 macrophages. In CM-iNOS-KO mice, CD68 expression is similar to that observed in control mice, as is infarct-specific elevation of iNOS expression. As before, no colocalization of iNOS and CD68 was observed. A particularly interesting finding is shown in Figure 22, where large regions of the epicardial portion of the heart continue to express cTnT, but visible fiber orientation appears to be longitudinal, rather than circumferential.

In all histological assessments of hearts extracted from post-MI day 28 mice, CD206 infiltration into the infarct region was observed at very high densities. In both MP-iNOS-KO and CM-iNOS-KO mice, infarcts appear to be discontinuous or at least experience large regions of viable cardiomyocytes, as determined by 647nm fluorescence and shown in Figure 23 and Figure 24. In the heart extracted from a macrophage-knockout mouse, iNOS expression in the infarct and border regions appear elevated based on fluorescence, while such elevated expression is not observed in hearts from cardiomyocyte-specific knockout mice. In both CM-iNOS-KO mice, CD68 expression is still observed primarily within the border zone, with little to no colocalization with iNOS expression. As at day 7, infarcts appear to be sparse or mixed with regions of viable cardiomyocytes in both CM-iNOS-KO and MP-iNOS-KO hearts.

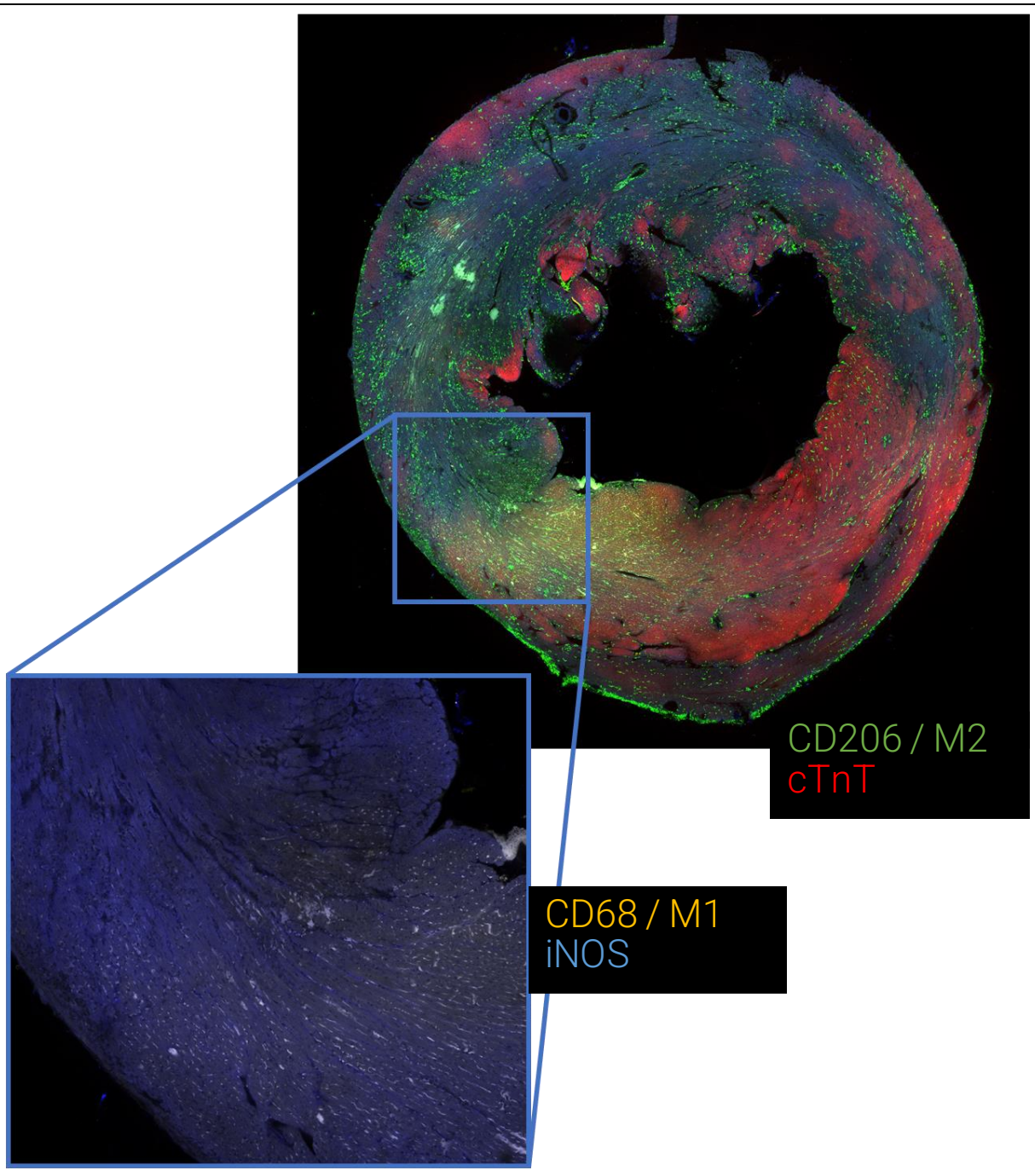

Figure 19. IHC in iNOS-FL Heart at Day 2 Post-MI. Channel definitions: cTnT: Red; CD206: Green; CD68: Yellow; iNOS: Blue. At day 2 post-MI, iNOS and CD68 are observed to colocalize in the border zone but are not observed in the infarct region.

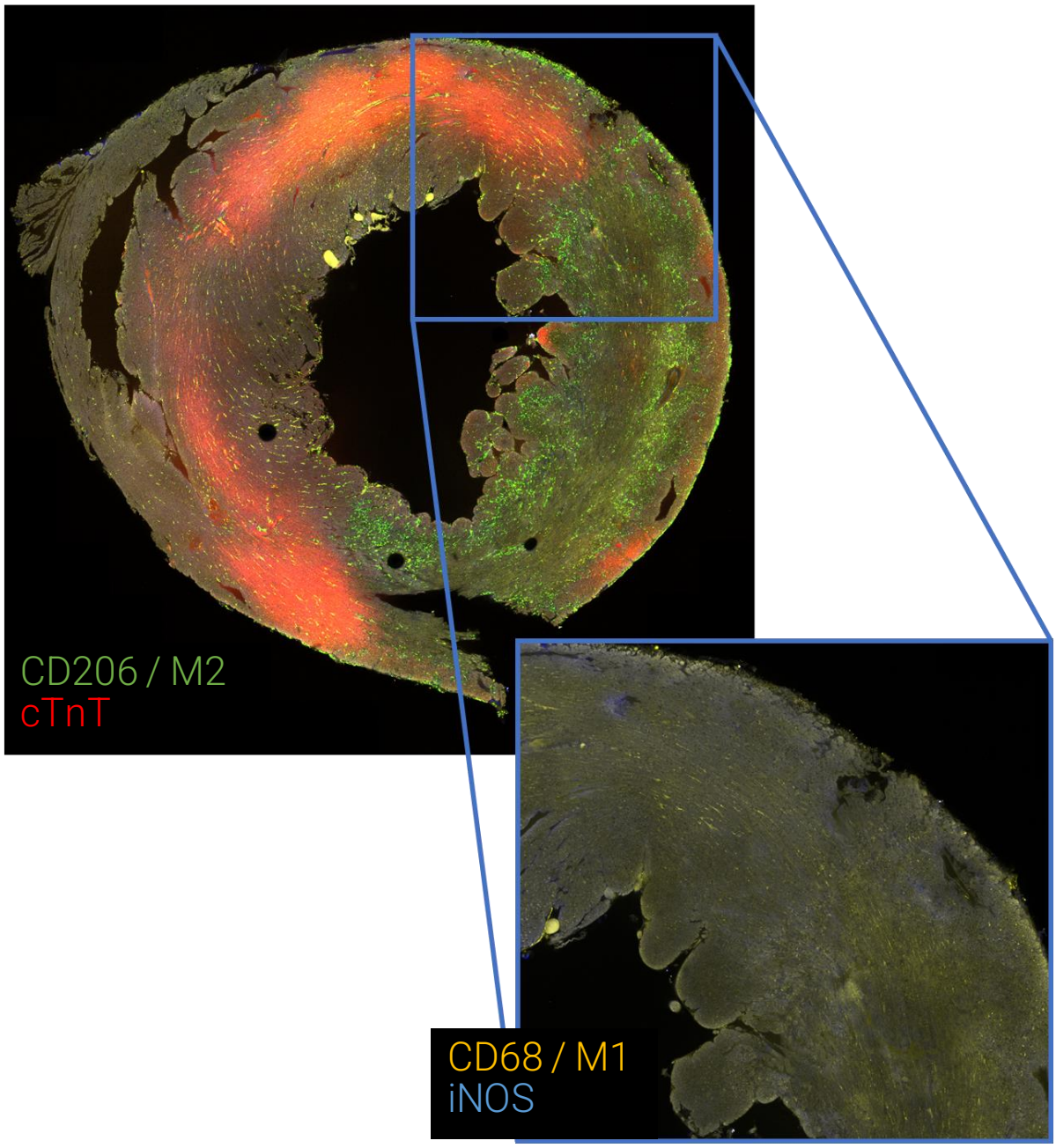

Figure 20. IHC in MΦ-iNOS-KO Heart at Day 2 Post-MI. Compared to control mice, elevated iNOS expression is not observed, even in regions with CD68-expressing cells, confirming successful knockout in those cell types.

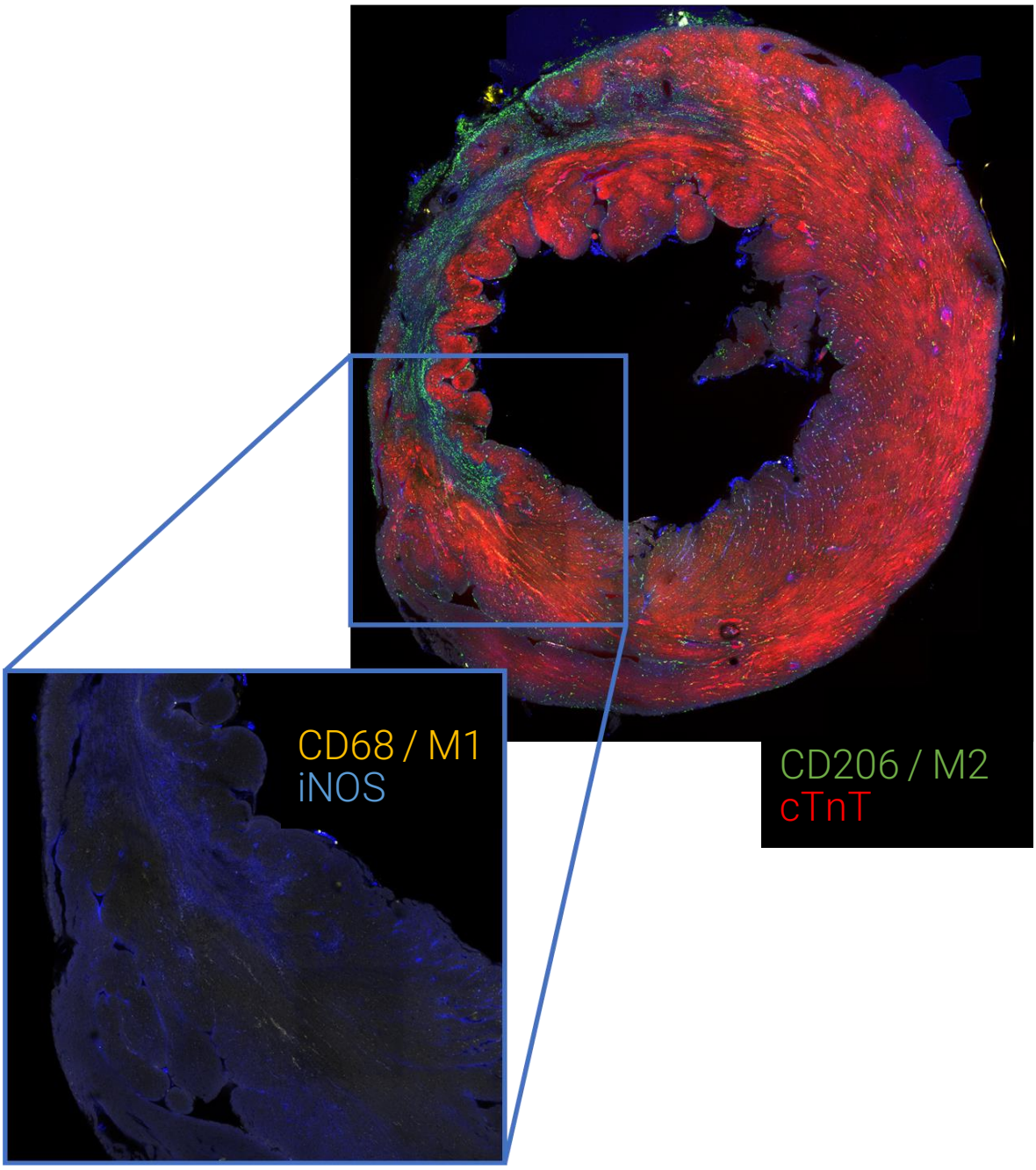

Figure 21. IHC in iNOS-FL Heart at Day 7 Post-MI. CD206-expressing macrophages are now present throughout the infarct region, while CD68-expressing cells have reduced in quantity compared to day 2. iNOS expression in the infarct, however, is now elevated.

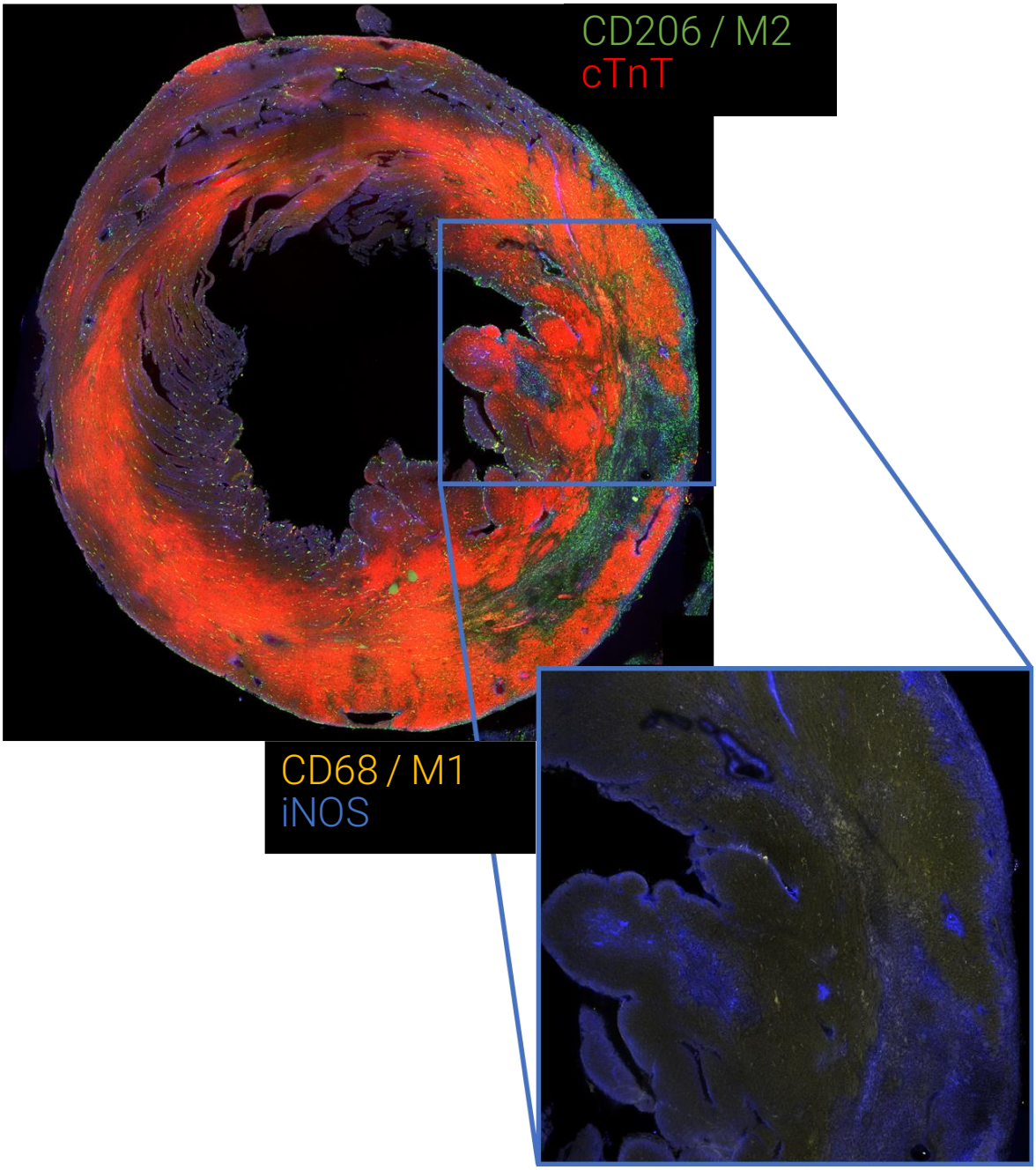

Figure 22. IHC in CM-iNOS-KO Heart at Day 7 Post-MI. CD206-expressing macrophages are now present throughout the infarct region, similar to iNOS-FL mice. Compared to iNOS-FL, iNOS expression in the borderzone vs infarct is far lower, suggesting that cardiomyocytes are producing iNOS in the borderzone of control mice at day 7.

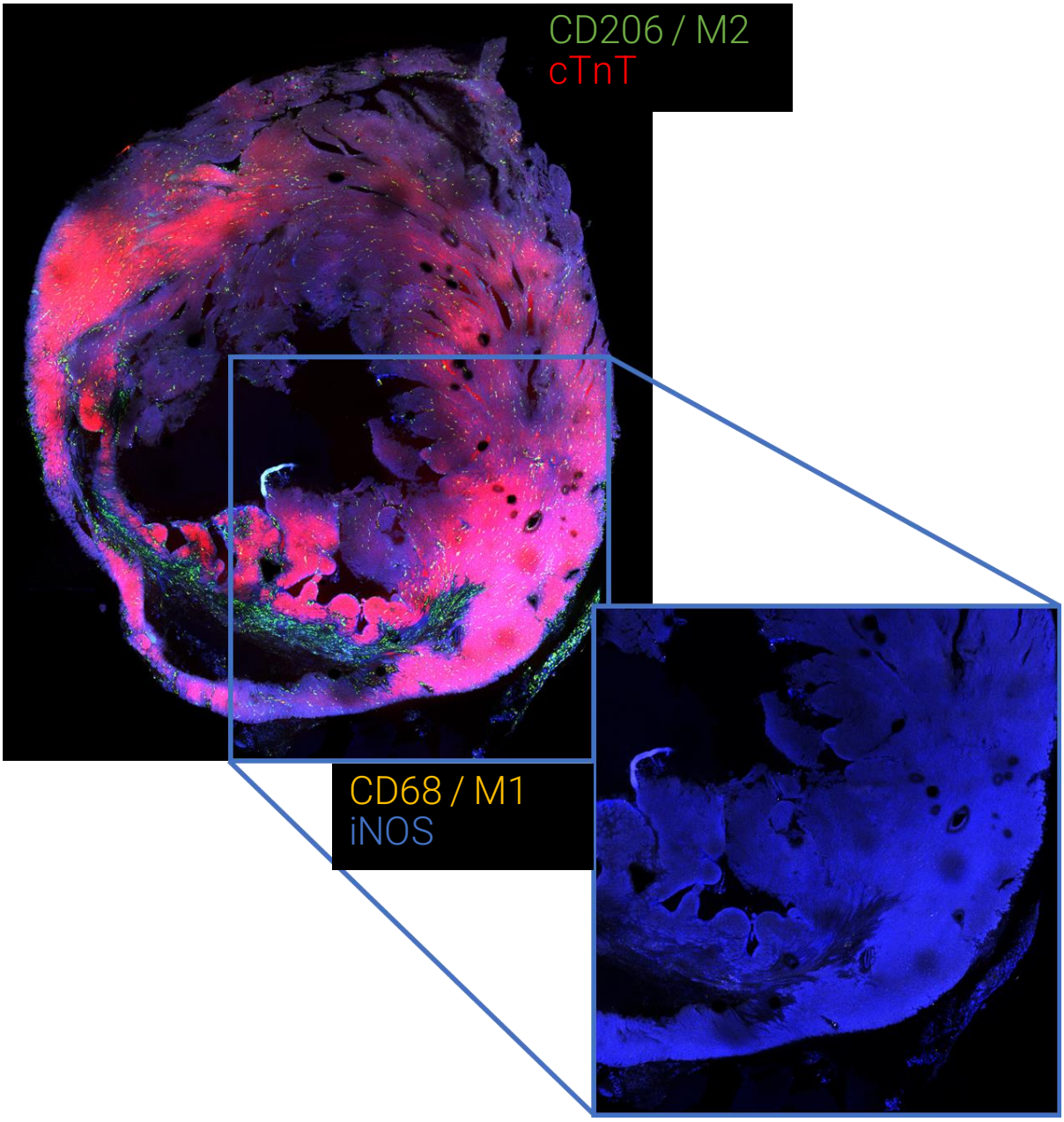

Figure 23. IHC in MΦ-iNOS-KO Heart at Day 28 Post-MI. Infarct region partially separated during slicing. Note presence of CD206 in the infarct region remains elevated, while no CD68 expression was detected. iNOS expression shows no regional bias towards the infarct.

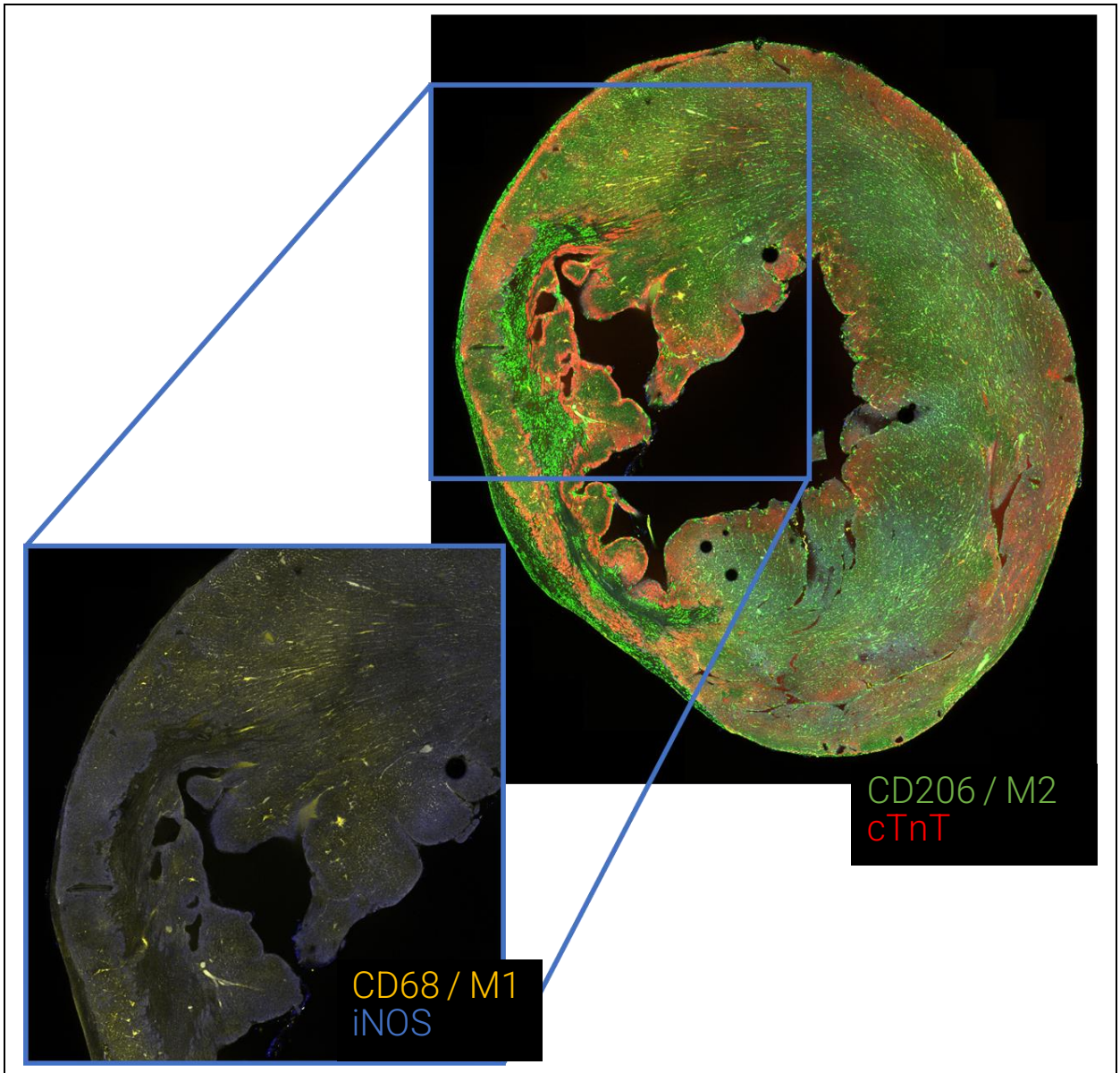

Figure 24. IHC in CM-iNOS-KO Heart at Day 28 Post-MI. A continuous segment of viable cardiomyocytes appears within infarcted sectors. CD206-expressing cells are still concentrated heavily within the infarct, while CD68 expression is exhibited in the border zone. iNOS expression is minimal and shows no colocalization with any other stain.

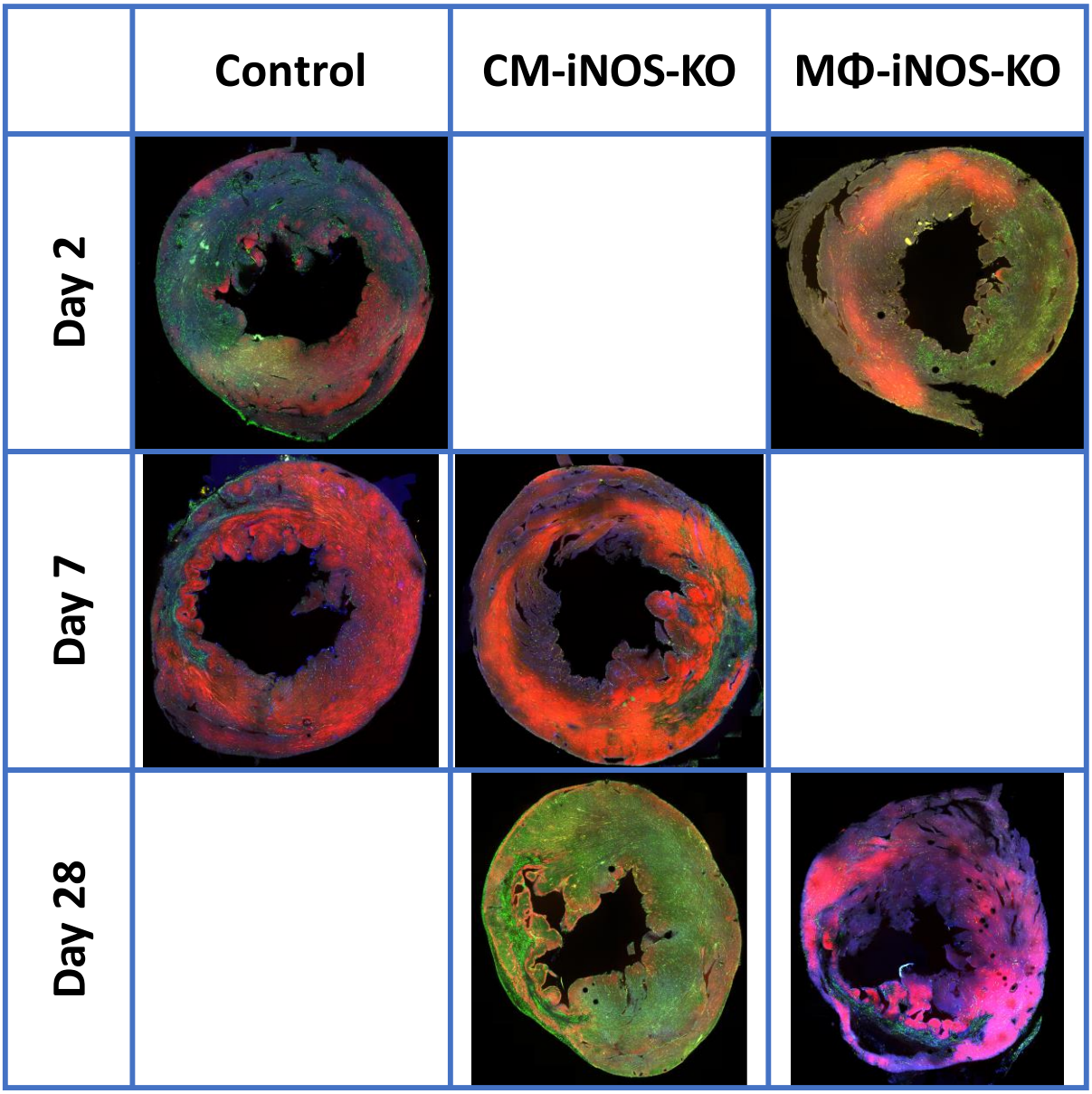

Figure 25. Histological staining of cleared cardiac sections. Cardiac sections stained for CD206 (green), cTnT (red), CD68 (yellow), and iNOS (blue). Slices were mounted and imaged on a confocal laser scanning microscope (Leica Microsystems; Wetzlar, Germany). Staining for cTnT is used to identify the location of the infarct region.

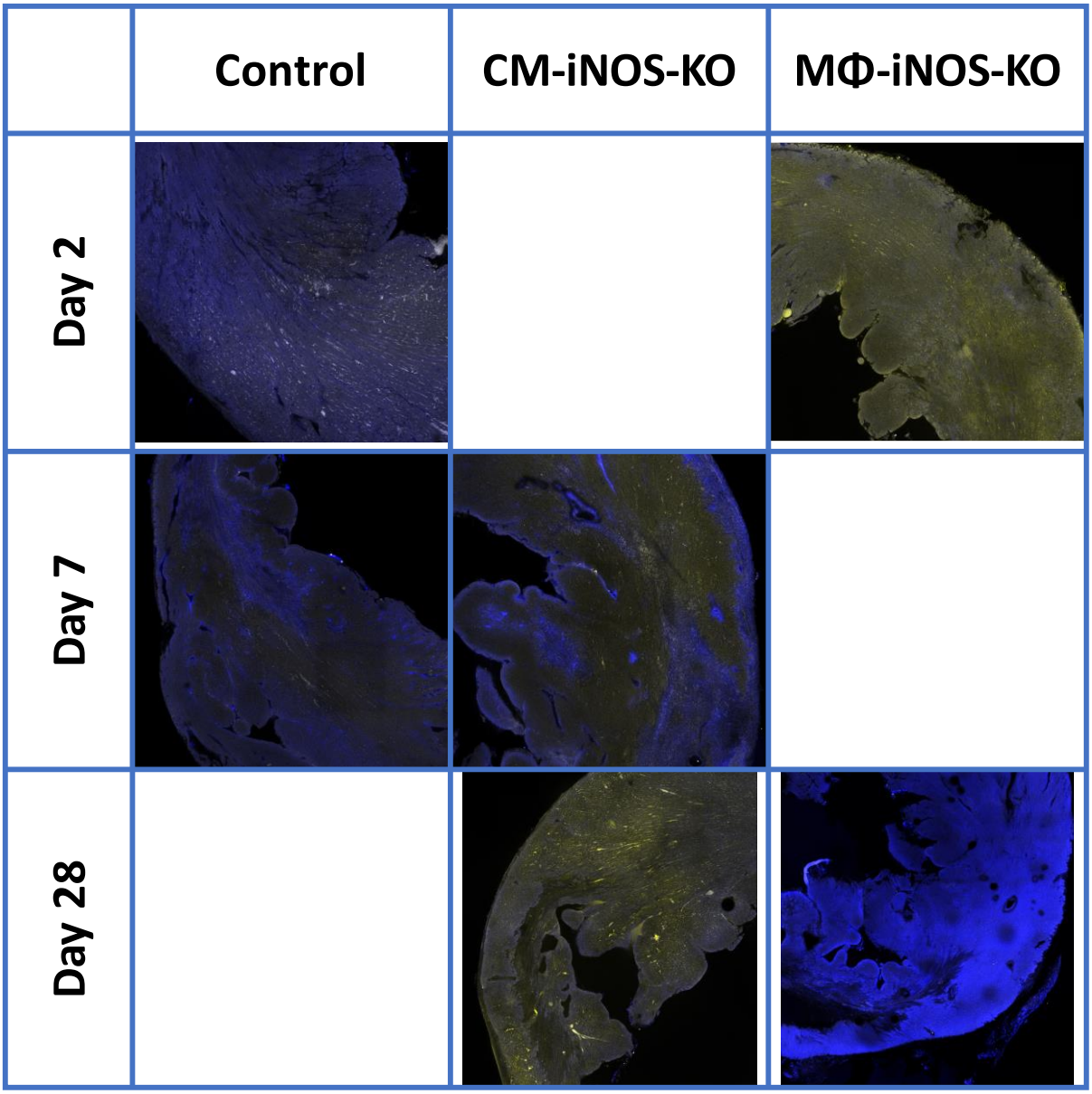

Figure 26. Histological staining of the border zone. Cardiac sections stained for iNOS (blue) and CD68 (yellow). Images are taken from whole-section histological slides, displaying only two channels to improve visibility of the effects. All slices were stained for CD206 and cTnT expression (Figure 25) to assess location of the border zone. Images are presented using raw values.

	Control	CM-iNOS-KO	MΦ-iNOS-KO
Day 2	• Elevated iNOS and CD68 border zone presence • Strong colocalization of iNOS and CD68 • Low CD206 presence in the infarct region		• Limited iNOS expression • No colocalization of iNOS and CD68 • Low CD206 presence in the infarct region
Day 7	• No observation of CD68 • Elevated CD206 presence in the infarct region • Initial onset of wall thinning	• Decreased iNOS presence in border zone vs infarct • Elevated presence of CD68 in myocardium • Reduced thinning of infarct	
Day 28		• Decreased iNOS presence throughout sample • Elevated presence of CD68+ macrophages throughout myocardium • Thinned infarct with layers of cTnT+ cardiomyocytes	• Broadly non-regional elevated iNOS presence • No observation of CD68 • Thin, fragile infarct region • Elevated CD206 presence in the infarct

Figure 26. Summary of histological observations. Summary of observations from histological analysis, grouped by treatment group and timepoint for quick reference.

Discussion

Alterations in cardiac volumes and function are considered within the context of a prior study performed by our lab studying the impact of global iNOS knockout on post-MI remodeling and cardiac function[100]. While a global knockout resulted in less expansion of both EDV and ESV, as well as EF, the cell-specific knockout approach implemented here resulted in lower magnitude of effect, with a difference of only 12% or 15% in MP-iNOS-KO or CM-iNOS-KO groups relative to baseline at day 7, which was the largest separation between the groups. By day 28, the separation between groups had largely diminished within the cell type-specific knockouts, which differs from our previous finding in global knockouts. Ejection fraction shows similar trends in cell type-specific knockouts in the early stages of post-MI recovery, with MP-iNOS-KO and CM-iNOS-KO groups slowing the rate at which EF worsened based on mean EF% at days 2 and 7, while day 28 results were similar to those observed in control mice. This differs from the lack of notable decrease in EF after day 1 post-MI in the global knockout model.

The differences in wall thickness between mice provides a unique picture of the physiological changes on the heart. The infarct region of remains much less impacted by thinning in CM-iNOS-KO mice throughout the entirety of recovery, and the entire myocardium is slightly more resistant to wall thinning during late remodeling. This could be due to increased edematous swelling during the inflammatory and proliferative phases, with some additional resistance to wall thinning during maturation. Both MP-iNOS-KO and control mice present very similar changes in wall thickness in each region and timepoint, with the only noteworthy difference observed in the remote region at day 2 post-MI. The stark difference observed in the CM-iNOS-KO group suggests that loss of cardiomyocyte mass in the infarct region may be impacted by the expression of iNOS by cardiomyocytes within the area at risk. The lack of a similar observation in MP-iNOS-KO mice

suggests that extended release of iNOS by impacted cardiomyocytes may have a more dominant effect on cardiomyocyte loss in the long-term.

Circumferential strains in the infarct, border, and remote regions, as assessed by both manual alignment and CoCaToo automated alignment, suggest that lack of iNOS expression from an individual cell type does not result in either improved or worsened regional function in the infarct. However, in CM-iNOS-KO mice, peak border and remote region function failed to recover in a similar manner to what was observed in both macrophage knockouts and control mice. Paired with the apparently higher retention of cardiomyocytes based on myocardial wall thickness, this suggests that, while retained, cardiomyocyte functionality is still heavily impacted. The impact of increased cardiomyocyte retention on infarct stiffness could result in altered stress at the border zone during the cardiac cycle, altering remodeling and function over time[107,108].

Comparison of the results from manual alignment to automated model-based co-registration shows that infarct region results are highly similar, suggesting effective coregistration of the infarct and strain maps. Border zone and remote region comparisons depict a generally lower-magnitude strain result at all points when assessed via CoCaToo, which is likely the result of more frequent sampling points throughout the myocardium. As the sector-based assessment uses only 6 sectors spread out across equal angular extent in the myocardium, regions defined as “remote” tend to be more widely separated from the infarct region. Due to the infarct percent necessary for a sector to be labeled as an “infarct” sector, remote sectors may not even occur within a given short-axis slice, instead containing only infarct and adjacent sectors. The 3-dimensional interpolation process and far finer control over border zone width in the model results in far less frequent cases of mice having no elements defined as remote. As these mice would have the largest infarct percentages and would therefore be suggested to have the most heavily impaired regional function, it is

reasonable that inclusion of these subjects by CoCaToo would produce lower-magnitude strains. Similarly, while border zone sectors will tend to occupy at least one full sector of the heart and may be separated by several degrees from the edge of the infarct region indicated by LGE, border elements will be placed immediately adjacent to the infarct elements when using automated alignment, which will also be likely to reduce peak strains when averaged across elements.

The results from the CoCaToo platform for automated confocal alignment and quantification were beset with multiple challenges which prevented successful fitting and assessment. A major factor was low slice counts and few animals for assessment, necessitating the use of less ideal images for fitting attempts. While slices were selected such that contour formation was possible in all cases, uneven fluorescence occurred in some cases that were used due to low N. Slice spacing was inconsistent due to slice exclusions for a variety of causes, leaving interpolation to be performed across large spans of myocardium. Cross-slice brightness was also a factor, which can result from slight changes in permeability of the tissue samples to the staining antibodies, potentially as a result of altered incubation times in CUBIC-I reagent necessary to reach optical clarity. These factors together result in a set of inputs which are poorly suited to the goal of automated fluorescence processing for quantitative histology. A method which may be promising to mitigate inter-slice variability in fluorophore brightness is to utilize more complex normalization methods, which aim to reduce the effect of confounding factors on brightness variation in histological samples[109].

While not well-suited to automated processing, the histological results are generally expected outcomes. Control mice exhibit colocalization of iNOS and CD68 at the early inflammatory stage of the post-MI response, while macrophage-knockout mice do not, and seem to exhibit lower iNOS concentrations in the early infarct, but hearts harvested well after the end of the inflammatory

response do seem to be expressing iNOS within the infarct. Cardiomyocyte-specific knockouts present with apparently elevated iNOS concentration in the infarct early after MI, while later expression is low with no apparent sites of elevated expression. CD206 infiltration appeared similar in all samples assessed at each timepoint post-MI, from initial borderzone presence early after MI to widespread infiltration by day 7 and continuing onto day 28.

Conclusions

The findings of this study suggest that the previously-identified impacts of iNOS knockout on LV remodeling post-MI are not the result of the contributions of a single cell type. However, the impacts of individual cell type knockout does result in some notable variance in outcomes, particularly in the elevated edematous swelling of the infarct immediately after infarction and the progression of thinning in the infarct region. Additionally, the results of the model-based automated co-registration of CMR endpoints are encouraging that the combined cardiac model is a capable tool for post-MI analysis, which has the potential to improve consistency in result analysis through the reduction of intra-user variability in sector alignment and classification.

Limitations and Future Directions

The most obvious limitation of the study is sample size. Early mortality in treatment groups resulted in high mortality of limited-availability mice due to the later results of breeder colony litters. The thresholds of mouse weight established after observing the elevated mortality could be used to perform follow-up studies for increased power if combined with current results. Generally, the effects of cell type-specific knockout on remodeling trended towards the results established previously in global knockouts, but lower-magnitude changes overall resulted in an underestimate of power. Original estimates were based on observed day-28 changes in global knockouts, while day 7 impacts were higher-magnitude differences in cell type-specific knockouts.

Potential modifications to the histological protocol could also be utilized to improve the potential for quantitative histology. A potential tool for this could be Glowing Galbumin™ (BioPAL, Inc.; Worcester, MA), a gadolinium-labeled albumin that is co-labeled with a fluorophore for fluorescence imaging. This could provide a landmark for automated co-registration of histological samples after MI, which does not require antibody staining procedures. Confirmation of compatibility with the CSAC staining protocol would be a necessary intermediate step, along with a comparison of post-injection dynamics versus Gd-DTPA alone for proper timing of LGE sequences.

An additional potential modification to the automated platform is the implementation of a thresholding approach to quantitative histology. Rather than using averaged fluorescence for quantitation, image data could be compressed using a summation approach, instead producing a value of {1} for each pixel which lies above the automated threshold. The end-result would be less prone to brightness variation across samples due to in-slice thresholding but would produce a more abstracted result when compared to direct fluorescence. A major strength of such an algorithm would be greater scalability without as much feature loss overall as traditional compression. Direct image compression produces a smoothing effect, which can wash out local minima and maxima towards a regional average. A summation-based compression would preserve the exact impact of individual pixels even with extremely high compression ratios and could be implemented as a recursive algorithm with pre-determined endpoint resolutions for simple integration into automated contour alignment. In the present study, I desired to utilize fluorescence intensity as a variable, but results suggest that the available imaging tools are not sufficient to produce consistent enough fluorescence results to incorporate these as raw inputs to an interpolation algorithm.

Incorporation of advanced normalization methods to reduce inter-slice variability could improve performance of the model in this regard and increase its power as a diagnostic tool.

Related to histological model advancements, use of a whole-mount light-sheet fluorescence microscopy system could produce much more complete histological image stacks. Conversion to such a system would require extended incubation periods and larger volumes of antibody usage, but LSFM remains the gold standard for thick-section or whole-mount organ microscopy. This would offset both the cross-sample fluorescence variability and significantly reduce necessary alignment steps. It would also eliminate or significantly reduce the prevalence of malformed samples for microscopy, reducing the number of subjects necessary to gather clear and complete histological results.

REFERENCES

1. Yu, B., Akushevich, I., Yashkin, A. P. & Kravchenko, J. Epidemiology of Geographic Disparities of Myocardial Infarction Among Older Adults in the United States: Analysis of 2000–2017 Medicare Data. *Front. Cardiovasc. Med.* **8**, (2021).

2. Bishu, K. G. *et al.* Estimating the Economic Burden of Acute Myocardial Infarction in the US: 12 Year National Data. *Am. J. Med. Sci.* **359**, 257–265 (2020).

3. Faridi, K. F. *et al.* New Heart Failure After Myocardial Infarction (From the National Cardiovascular Data Registries [NCDR] Linked With All-Payer Claims). *Am. J. Cardiol.* **151**, 70–77 (2021).

4. White, H. D. *et al.* Left ventricular end-systolic volume as the major determinant of survival after recovery from myocardial infarction. *Circulation* **76**, 44–51 (1987).

5. Migrino, R. *et al.* End-systolic volume index at 90 to 180 minutes into reperfusion therapy for acute myocardial infarction is a strong predictor of early and late mortality. The Global Utilization of Streptokinase and t-PA for Occluded Coronary Arteries (GUSTO)-I Angiographic Investigators. *Circulation* **96**, 116–121 (1997).

6. Lee, T. H. *et al.* Impact of left ventricular cavity size on survival in advanced heart failure. *Am. J. Cardiol.* **72**, 672–676 (1993).

7. Solomon, S. D. *et al.* Changes in Ventricular Size and Function in Patients Treated With Valsartan, Captopril, or Both After Myocardial Infarction. *Circulation* **111**, 3411–3419 (2005).

8. Watzinger, N. *et al.* The potential of contrast-enhanced magnetic resonance imaging for predicting left ventricular remodeling. *J. Magn. Reson. Imaging JMRI* **16**, 633–640 (2002).

9. Pfeffer, M. A. & Braunwald, E. Ventricular remodeling after myocardial infarction. Experimental observations and clinical implications. *Circulation* **81**, 1161–1172 (1990).

10. McKay, R. G. *et al.* Left ventricular remodeling after myocardial infarction: a corollary to infarct expansion. *Circulation* **74**, 693–702 (1986).

11. Chareonthaitawee, P., Christian, T. F., Hirose, K., Gibbons, R. J. & Rumberger, J. A. Relation of initial infarct size to extent of left ventricular remodeling in the year after acute myocardial infarction. *J. Am. Coll. Cardiol.* **25**, 567–573 (1995).

12. Lee, A. W. C., Costa, C. M., Strocchi, M., Rinaldi, C. A. & Niederer, S. A. Computational Modeling for Cardiac Resynchronization Therapy. *J Cardiovasc. Transl. Res.* **11**, 92–108 (2018).

13. Phung, T.-K. N., Waters, C. D. & Holmes, J. W. Open-Source Routines for Building Personalized Left Ventricular Models From Cardiac Magnetic Resonance Imaging Data. *J. Biomech. Eng.* **142**, (2019).

14. Shah, S. A. *et al.* Nitroxide-enhanced MRI of cardiovascular oxidative stress. *NMR Biomed.* **33**, e4359 (2020).

15. Gilson, W. D. *et al.* Borderzone contractile dysfunction is transiently attenuated and left ventricular structural remodeling is markedly reduced following reperfused myocardial infarction in inducible nitric oxide synthase knockout mice. *J. Am. Coll. Cardiol.* **50**, 1799–1807 (2007).

16. Perazzolo Marra, M., Lima, J. A. C. & Iliceto, S. MRI in acute myocardial infarction. *Eur. Heart J.* **32**, 284–293 (2011).

17. Sosnovik, D. E. *et al.* Diffusion Spectrum MRI Tractography Reveals the Presence of a Complex Network of Residual Myofibers in Infarcted Myocardium. *Circ. Cardiovasc. Imaging* **2**, 206–212 (2009).

18. Yan, A. T. *et al.* Characterization of the Peri-Infarct Zone by Contrast-Enhanced Cardiac Magnetic Resonance Imaging Is a Powerful Predictor of Post–Myocardial Infarction Mortality. *Circulation* **114**, 32–39 (2006).

19. Saeed, M. *et al.* Magnetic Resonance Characterization of the Peri-Infarction Zone of Reperfused Myocardial Infarction With Necrosis-Specific and Extracellular Nonspecific Contrast Media. *Circulation* **103**, 871–876 (2001).

20. Mojsejenko, D. *et al.* Estimating passive mechanical properties in a myocardial infarction using MRI and finite element simulations. *Biomech. Model. Mechanobiol.* **14**, 633–647 (2015).

21. Sun, K. *et al.* A Computationally Efficient Formal Optimization of Regional Myocardial Contractility in a Sheep With Left Ventricular Aneurysm. *J. Biomech. Eng.* **131**, (2009).

22. Moustakidis, P. *et al.* Altered Left Ventricular Geometry Changes the Border Zone Temporal Distribution of Stress in an Experimental Model of Left Ventricular Aneurysm: A Finite Element Model Study. *Circulation* **106**, I–168 (2002).

23. Guccione, J. M. *et al.* Mechanism underlying mechanical dysfunction in the border zone of left ventricular aneurysm: a finite element model study. *Ann. Thorac. Surg.* **71**, 654–662 (2001).

24. Jc, W. *et al.* MRI-based finite-element analysis of left ventricular aneurysm. *Am. J. Physiol. Heart Circ. Physiol.* **289**, (2005).

25. Wenk, J. F. *et al.* Regional Left Ventricular Myocardial Contractility and Stress in a Finite Element Model of Posterobasal Myocardial Infarction. *J. Biomech. Eng.* **133**, (2011).

26. Boyle, M. P. & Weisman, H. F. Limitation of infarct expansion and ventricular remodeling by late reperfusion. Study of time course and mechanism in a rat model. *Circulation* **88**, 2872–2883 (1993).

27. Lee, L. C. *et al.* A Novel Method for Quantifying In-Vivo Regional Left Ventricular Myocardial Contractility in the Border Zone of a Myocardial Infarction. *J. Biomech. Eng.* **133**, (2011).

28. Shimkunas, R. *et al.* Left Ventricular Myocardial Contractility Is Depressed in the Borderzone After Posterolateral Myocardial Infarction. *Ann. Thorac. Surg.* **95**, 1619–1625 (2013).

29. van Zuylen, V.-L. *et al.* Myocardial infarction models in NOD/Scid mice for cell therapy research: permanent ischemia vs ischemia–reperfusion. *SpringerPlus* **4**, 336 (2015).

30. Pluijmert, N. J., Bart, C. I., Bax, W. H., Quax, P. H. A. & Atsma, D. E. Effects on cardiac function, remodeling and inflammation following myocardial ischemia–reperfusion injury or unreperfused myocardial infarction in hypercholesterolemic APOE*3-Leiden mice. *Sci. Rep.* **10**, 16601 (2020).

31. Oerlemans, M. I. F. J. *et al.* Inhibition of RIP1-dependent necrosis prevents adverse cardiac remodeling after myocardial ischemia–reperfusion in vivo. *Basic Res. Cardiol.* **107**, 270 (2012).

32. Herz, S. L., Ingrassia, C. M., Homma, S., Costa, K. D. & Holmes, J. W. Parameterization of left ventricular wall motion for detection of regional ischemia. *Ann. Biomed. Eng.* **33**, 912–919 (2005).

33. Heiberg, E. *et al.* Design and validation of Segment - freely available software for cardiovascular image analysis. *BMC Med. Imaging* **10**, 1 (2010).

34. Nielsen, P. M., Le Grice, I. J., Smaill, B. H. & Hunter, P. J. Mathematical model of geometry and fibrous structure of the heart. *Am. J. Physiol.-Heart Circ. Physiol.* **260**, H1365–H1378 (1991).

35. Hunter, P. J. & Smaill, B. H. The analysis of cardiac function: A continuum approach. *Prog. Biophys. Mol. Biol.* **52**, 101–164 (1988).

36. Engblom, H. *et al.* A new automatic algorithm for quantification of myocardial infarction imaged by late gadolinium enhancement cardiovascular magnetic resonance: experimental validation and comparison to expert delineations in multi-center, multi-vendor patient data. *J. Cardiovasc. Magn. Reson. Off. J. Soc. Cardiovasc. Magn. Reson.* **18**, 27 (2016).

37. Gilliam, A. D., Suever, J. D. & contributors. DENSEanalysis. (2021).

38. Spottiswoode, B. S. *et al.* Tracking Myocardial Motion From Cine DENSE Images Using Spatiotemporal Phase Unwrapping and Temporal Fitting. *IEEE Trans. Med. Imaging* **26**, 15–30 (2007).

39. Shin, S.-H. *et al.* Mechanical Dyssynchrony After Myocardial Infarction in Patients With Left Ventricular Dysfunction, Heart Failure, or Both. *Circulation* **121**, 1096–1103 (2010).

40. Blocker, S. J. *et al.* Ex Vivo MR Histology and Cytometric Feature Mapping Connect Three-dimensional in Vivo MR Images to Two-dimensional Histopathologic Images of Murine Sarcomas. *Radiol. Imaging Cancer* **3**, e200103 (2021).

41. Whitaker, J. *et al.* Improved co-registration of ex-vivo and in-vivo cardiovascular magnetic resonance images using heart-specific flexible 3D printed acrylic scaffold combined with non-rigid registration. *J. Cardiovasc. Magn. Reson.* **21**, 62 (2019).

42. Toga, A. W. *et al.* Postmortem cryosectioning as an anatomic reference for human brain mapping. *Comput. Med. Imaging Graph.* **21**, 131–141 (1997).

43. Oh, S. W. *et al.* A mesoscale connectome of the mouse brain. *Nature* **508**, 207–214 (2014).

44. Sands, G. B. *et al.* Automated imaging of extended tissue volumes using confocal microscopy. *Microsc. Res. Tech.* **67**, 227–239 (2005).

45. Rutherford, S. L., Trew, M. L., Sands, G. B., LeGrice, I. J. & Smaill, B. H. High-Resolution 3-Dimensional Reconstruction of the Infarct Border Zone. *Circ. Res.* **111**, 301–311 (2012).

46. Young, Legrice, Young, & Smaill. Extended confocal microscopy of myocardial laminae and collagen network. *J. Microsc.* **192**, 139–150 (1998).

47. Tsai, P. S., Friedman, B., Squier, J. & Kleinfeld, D. Cutting Tissue With Ultrashort Pulsed Laser Light. *Opt. Photonics News* **15**, 24–29 (2004).

48. Tsai, P. S. *et al.* Plasma-mediated ablation: an optical tool for submicrometer surgery on neuronal and vascular systems. *Curr. Opin. Biotechnol.* **20**, 90–99 (2009).

49. Ichimura, K. *et al.* Three-dimensional architecture of podocytes revealed by block-face scanning electron microscopy. *Sci. Rep.* **5**, 8993 (2015).

50. Spalteholz, W. *Ueber das Durchsichtigmachen von menschlichen und tierischen Praeparaten und seine theoretischen Bedingungen*. (S. Hirzel, 1914).

51. Dodt, H.-U. *et al.* Ultramicroscopy: three-dimensional visualization of neuronal networks in the whole mouse brain. *Nat. Methods* **4**, 331–336 (2007).

52. Hama, H. *et al.* Scale: a chemical approach for fluorescence imaging and reconstruction of transparent mouse brain. *Nat. Neurosci.* **14**, 1481–1488 (2011).

53. Hama, H. *et al.* ScaleS: an optical clearing palette for biological imaging. *Nat. Neurosci.* **18**, 1518–1529 (2015).

54. Ertürk, A. *et al.* Three-dimensional imaging of solvent-cleared organs using 3DISCO. *Nat. Protoc.* **7**, 1983–1995 (2012).

55. Ke, M.-T., Fujimoto, S. & Imai, T. SeeDB: a simple and morphology-preserving optical clearing agent for neuronal circuit reconstruction. *Nat. Neurosci.* **16**, 1154–1161 (2013).

56. Chung, K. *et al.* Structural and molecular interrogation of intact biological systems. *Nature* **497**, 332–337 (2013).

57. Kuwajima, T. *et al.* ClearT: a detergent- and solvent-free clearing method for neuronal and non-neuronal tissue. *Development* **140**, 1364–1368 (2013).

58. Weissleder, R. A clearer vision for in vivo imaging. *Nat. Biotechnol.* **19**, 316–317 (2001).

59. Matsumoto, K. *et al.* Advanced CUBIC tissue clearing for whole-organ cell profiling. *Nat. Protoc.* **14**, 3506–3537 (2019).

60. Susaki, E. A. *et al.* Advanced CUBIC protocols for whole-brain and whole-body clearing and imaging. *Nat. Protoc.* **10**, 1709–1727 (2015).

61. Susaki, E. A. *et al.* Whole-Brain Imaging with Single-Cell Resolution Using Chemical Cocktails and Computational Analysis. *Cell* **157**, 726–739 (2014).

62. Wang, Z. *et al.* Imaging transparent intact cardiac tissue with single-cell resolution. *Biomed. Opt. Express* **9**, 423–436 (2018).

63. Tainaka, K. *et al.* Whole-Body Imaging with Single-Cell Resolution by Tissue Decolorization. *Cell* **159**, 911–924 (2014).

64. Nehrhoff, I. *et al.* 3D imaging in CUBIC-cleared mouse heart tissue: going deeper. *Biomed. Opt. Express* **7**, 3716–3720 (2016).

65. Kuroda, M. & Kuroda, S. Whole-body clearing of beetles by successive treatment with hydrogen peroxide and CUBIC reagents. *Entomol. Sci.* **23**, 311–315 (2020).

66. Schindelin, J. *et al.* Fiji: an open-source platform for biological-image analysis. *Nat. Methods* **9**, 676 (2012).

67. Schneider, C. A., Rasband, W. S. & Eliceiri, K. W. NIH Image to ImageJ: 25 years of image analysis. *Nat. Methods* **9**, 671–675 (2012).

68. Witzenburg, C. M. & Holmes, J. W. Biomechanics of Myocardial Ischemia and Infarction. in *Biomechanics: Trends in Modeling and Simulation* (eds. Holzapfel, G. A. & Ogden, R. W.) 233–269 (Springer International Publishing, 2017). doi:10.1007/978-3-319-41475-1_6.

69. Kim, D., Gilson, W. D., Kramer, C. M. & Epstein, F. H. Myocardial Tissue Tracking with Two-dimensional Cine Displacement-encoded MR Imaging: Development and Initial Evaluation. *Radiology* **230**, 862–871 (2004).

70. Sengel, øv M. *et al.* Global Longitudinal Strain Is a Superior Predictor of All-Cause Mortality in Heart Failure With Reduced Ejection Fraction. *JACC Cardiovasc. Imaging* **8**, 1351–1359 (2015).

71. Buss, S. J. *et al.* Prediction of functional recovery by cardiac magnetic resonance feature tracking imaging in first time ST-elevation myocardial infarction. Comparison to infarct size and transmurality by late gadolinium enhancement. *Int. J. Cardiol.* **183**, 162–170 (2015).

72. Bonios, M. J. *et al.* Value of apical circumferential strain in the early post-myocardial infarction period for prediction of left ventricular remodeling. *Hell. J. Cardiol. HJC Hell. Kardiologike Epitheorese* **55**, 305–312 (2014).

73. Khan, J. N. *et al.* Relationship of Myocardial Strain and Markers of Myocardial Injury to Predict Segmental Recovery After Acute ST-Segment–Elevation Myocardial Infarction. *Circ. Cardiovasc. Imaging* **9**, e003457 (2016).

74. McComb, C. *et al.* Assessment of the relationships between myocardial contractility and infarct tissue revealed by serial magnetic resonance imaging in patients with acute myocardial infarction. *Int. J. Cardiovasc. Imaging* **31**, 1201–1209 (2015).

75. Frangogiannis, N. G. The Mechanistic Basis of Infarct Healing. *Antioxid. Redox Signal.* **8**, 1907–1939 (2006).

76. Hume, R. D. & Chong, J. J. H. The Cardiac Injury Immune Response as a Target for Regenerative and Cellular Therapies. *Clin. Ther.* **42**, 1923–1943 (2020).

77. Li, W. *et al.* Heart-resident CCR2^{+} macrophages promote neutrophil extravasation through TLR9/MyD88/CXCL5 signaling. *JCI Insight* **1**, (2016).

78. Richardson, W., Clarke, S., Quinn, T. & Holmes, J. Physiological Implications of Myocardial Scar Structure. *Compr. Physiol.* **5**, 1877–1909 (2015).

79. Prabhu, S. D. & Frangogiannis, N. G. The Biological Basis for Cardiac Repair After Myocardial Infarction. *Circ. Res.* **119**, 91–112 (2016).

80. Rondeaux, J. *et al.* Ezh2 emerges as an epigenetic checkpoint regulator during monocyte differentiation limiting cardiac dysfunction post-MI. *Nat. Commun.* **14**, 4461 (2023).

81. Yakupova, E. I., Maleev, G. V., Krivtsov, A. V. & Plotnikov, E. Y. Macrophage polarization in hypoxia and ischemia/reperfusion: Insights into the role of energetic metabolism. *Exp. Biol. Med.* **247**, 958–971 (2022).

82. Nahrendorf, M. *et al.* The healing myocardium sequentially mobilizes two monocyte subsets with divergent and complementary functions. *J. Exp. Med.* **204**, 3037–3047 (2007).

83. Varasteh, Z. *et al.* In vivo Visualization of M2 Macrophages in the Myocardium After Myocardial Infarction (MI) Using 68Ga-NOTA-Anti-MMR Nb: Targeting Mannose Receptor (MR, CD206) on M2 Macrophages. *Front. Cardiovasc. Med.* **9**, 889963 (2022).

84. Yang, F. *et al.* Myocardial infarction and cardiac remodelling in mice. *Exp. Physiol.* **87**, 547–555 (2002).

85. Barandon, L. *et al.* Secreted Frizzled-Related Protein-1 Improves Postinfarction Scar Formation Through a Modulation of Inflammatory Response. *Arterioscler. Thromb. Vasc. Biol.* **31**, e80–e87 (2011).

86. Sarapultsev, A. P. *et al.* Modulation of Inflammatory Response Improves Myocardial Infarct Healing in Rats. *Curr. Pharm. Des.* **20**, 1980–1986 (2014).

87. Sugamura, K. & Keaney, John F. Reactive oxygen species in cardiovascular disease. *Free Radic. Biol. Med.* **51**, 978–992 (2011).

88. Balligand, J.-L. *et al.* Nitric Oxide-dependent Parasympathetic Signaling Is Due to Activation of Constitutive Endothelial (Type III) Nitric Oxide Synthase in Cardiac Myocytes ∗. *J. Biol. Chem.* **270**, 14582–14586 (1995).

89. Liu, V. W. T. & Huang, P. L. Cardiovascular roles of nitric oxide: A review of insights from nitric oxide synthase gene disrupted mice†. *Cardiovasc. Res.* **77**, 19–29 (2008).

90. Schulz, R., Nava, E. & Moncada, S. Induction and potential biological relevance of a Ca(2+)-independent nitric oxide synthase in the myocardium. *Br. J. Pharmacol.* **105**, 575–580 (1992).

91. Takimoto, Y. *et al.* Differential expression of three types of nitric oxide synthase in both infarcted and non-infarcted left ventricles after myocardial infarction in the rat. *Int. J. Cardiol.* **76**, 135–145 (2000).

92. Tian, B., Liu, J., Bitterman, P. B. & Bache, R. J. Mechanisms of cytokine induced NO-mediated cardiac fibroblast apoptosis. *Am. J. Physiol. Heart Circ. Physiol.* **283**, H1958-1967 (2002).

93. Robinson, N. M. K., Westmore, K. R., Martin, J. F., Emson, P. & Charles, I. G. Inducible Nitric Oxide Synthase Gene Transcription and Protein Activity in the Rat Heart during Endotoxaemia. *Biochem. Biophys. Res. Commun.* **231**, 211–216 (1997).

94. Vejlstrup, N. G. *et al.* Inducible Nitric Oxide Synthase (iNOS) in the Human Heart: Expression and Localization in Congestive Heart Failure. *J. Mol. Cell. Cardiol.* **30**, 1215–1223 (1998).

95. Haywood, G. A. *et al.* Expression of Inducible Nitric Oxide Synthase in Human Heart Failure. *Circulation* **93**, 1087–1094 (1996).

96. Xie, Q. *et al.* Cloning and Characterization of Inducible Nitric Oxide Synthase from Mouse Macrophages. *Science* **256**, 225–228 (1992).

97. Balligand, J.-L. & Cannon, P. J. Nitric Oxide Synthases and Cardiac Muscle. *Arterioscler. Thromb. Vasc. Biol.* **17**, 1846–1858 (1997).

98. Roy, R., Wilcox, J., Webb, A. J. & O'Gallagher, K. Dysfunctional and Dysregulated Nitric Oxide Synthases in Cardiovascular Disease: Mechanisms and Therapeutic Potential. *Int. J. Mol. Sci.* **24**, 15200 (2023).

99. Otani, H. The Role of Nitric Oxide in Myocardial Repair and Remodeling. *Antioxid. Redox Signal.* **11**, 1913–1928 (2009).

100. Gilson, W. D. *et al.* Borderzone contractile dysfunction is transiently attenuated and left ventricular structural remodeling is markedly reduced following reperfused myocardial infarction in inducible nitric oxide synthase knockout mice. *J. Am. Coll. Cardiol.* **50**, 1799–1807 (2007).

101. Clausen, B. E., Burkhardt, C., Reith, W., Renkawitz, R. & Förster, I. Conditional gene targeting in macrophages and granulocytes using LysMcre mice. *Transgenic Res.* **8**, 265–277 (1999).

102. Abram, C. L., Roberge, G. L., Hu, Y. & Lowell, C. A. Comparative analysis of the efficiency and specificity of myeloid-Cre deleting strains using ROSA-EYFP reporter mice. *J. Immunol. Methods* **408**, 89–100 (2014).

103. Prasad, K.-M. R., Xu, Y., Yang, Z., Acton, S. T. & French, B. A. Robust cardiomyocyte-specific gene expression following systemic injection of AAV: in vivo gene delivery follows a Poisson distribution. *Gene Ther.* **18**, 43–52 (2011).

104. Ross, A. J. *et al.* Serial MRI evaluation of cardiac structure and function in mice after reperfused myocardial infarction. *Magn. Reson. Med.* **47**, 1158–1168 (2002).

105. Landau, S. & Everitt, B. S. *A Handbook of Statistical Analyses Using SPSS*. (Taylor & Francis, 2003).

106. Clasen, L. *et al.* Cardiac ischemia and reperfusion in mice: a comprehensive hemodynamic, electrocardiographic and electrophysiological characterization. *Sci. Rep.* **13**, 5693 (2023).

107. Leong, C. O. *et al.* Computational Modelling of the Effect of Infarct Stiffness on Regional Myocardial Mechanics. *Annu. Int. Conf. IEEE Eng. Med. Biol. Soc. IEEE Eng. Med. Biol. Soc. Annu. Int. Conf.* **2019**, 6952–6955 (2019).

108. Estrada, A. C., Yoshida, K., Clarke, S. A. & Holmes, J. W. Longitudinal Reinforcementof Acute Myocardial Infarcts Improves Function by Transmurally Redistributing Stretch and Stress. *J. Biomech. Eng.* **142**, 0210091–02100910 (2020).

109. Macenko, M. *et al.* A method for normalizing histology slides for quantitative analysis. in *2009 IEEE International Symposium on Biomedical Imaging: From Nano to Macro* 1107–1110 (2009). doi:10.1109/ISBI.2009.5193250.